REFERENCE: **SAF/O3M/KNMI/VR/003**
ISSUE: 2/2016
DATE: 1 March 2016
PAGES: 46

O3M SAF VALIDATION REPORT

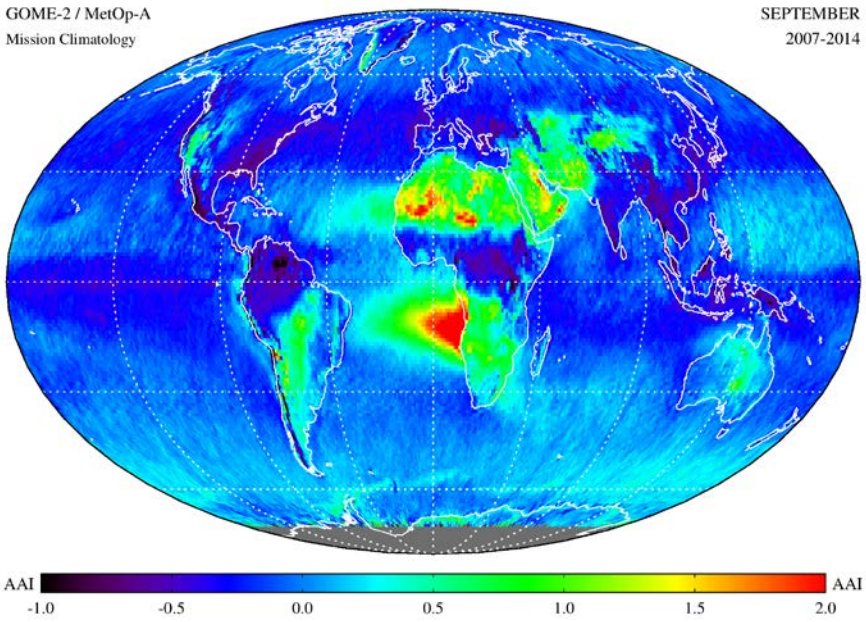

Reprocessed GOME-2 Absorbing Aerosol Index product

Product Identifier	Product Name
O3M-113	Reprocessed AAI from GOME-2A
O3M-179	Reprocessed AAI from GOME-2B
O3M-178	Reprocessed AAI from PMDs from GOME-2A
O3M-180	Reprocessed AAI from PMDs from GOME-2B

Authors	Institute
L.G. Tilstra	Royal Netherlands Meteorological Institute (KNMI)
O.N.E. Tuinder	Royal Netherlands Meteorological Institute (KNMI)
P. Stammes	Royal Netherlands Meteorological Institute (KNMI)

Document status sheet

Issue	Date	Page(s)	Modified Items / Reason for Change
1/2016	11-01-2016	all	first official version
2/2016	01-03-2016	all	changes and update after ORR

Contents

1 Introduction

1.1 Document purpose and scope

This document is the Validation Report (VR) for the reprocessed GOME-2 Absorbing Aerosol Index (AAI) products produced at KNMI in the framework of the O3M SAF (Satellite Application Facility on Ozone and Atmospheric Chemistry Monitoring). The aim of this VR is to present the outcome of the validation study, and to report to the users the quality that they may expect.

1.2 O3M SAF

The EUMETSAT Satellite Application Facility on Ozone and Atmospheric Chemistry Monitoring (O3M SAF) has been developed to provide good quality data for monitoring and research of atmospheric chemistry. More specifically, the O3M SAF processes, archives, validates and disseminates atmospheric data products of ozone, various trace gases such as SO_2 and NO_2, aerosols and surface ultraviolet radiation using the measurements performed by the Meteorological Operational (MetOp) satellites of EUMETSAT.

More information on the O3M SAF and available data can be found on the following web page:

http://o3msaf.fmi.fi/

1.3 Heritage

The Absorbing Aerosol Index (AAI) was originally developed to support the Total Ozone Mapping Spectrometer (TOMS) ozone retrieval algorithm [*Herman and Celarier*, 1997; *Torres et al.*, 1998]. TOMS measurements started in 1978, and a long data record of AAI from various satellite sensors is available for studies into the impact of aerosols on climate and trace gas retrievals.

The AAI has also been developed for the European satellite sensors GOME on ERS-2 [*de Graaf et al.*, 2005] and SCIAMACHY on Envisat [*Tilstra et al.*, 2012a]. The GOME-2 AAI discussed in this validation report is the direct descendant of the SCIAMACHY AAI product.

1.4 Processor and database versions

The processor versions and database versions of the reprocessed AAI product discussed in this VR are summarised in Tables 1 and 2 for MetOp-A and MetOp-B, respectively.

MetOp-A Time Period	PPF Version	PGE Version	Processing Type
2007–01–23 — 2014–06–17	5.3	1.35	reprocessed
2014–06–17 — 2015–06–25	6.0	1.35	reprocessed
2015–06–25 — 2015–11–30	6.1	1.35	reprocessed

Table 1: GOME-2/MetOp-A AAI: Overview of version numbers of the Product Processor Facility (PPF) and Product Generation Element (PGE) and time windows in which these were active.

MetOp-B Time Period	PPF Version	PGE Version	Processing Type
2012–12–12 — 2013–05–12	5.3	1.35	reprocessed
2014–06–17 — 2015–06–25	6.0	1.35	reprocessed
2015–06–25 — 2015–11–30	6.1	1.35	reprocessed

Table 2: GOME-2/MetOp-B AAI: Overview of version numbers of the Product Processor Facility (PPF) and Product Generation Element (PGE) and time windows in which these were active.

Please note that the time interval that applies to the PMD-AAI from MetOp-A does not start at 23-01-2007, but at 11-03-2008, because this is the date at which the PMD band definition was changed from v1.0 to v3.1. The PMD-AAI from PMD band definition v1.0 is not compatible with the PMD-AAI from PMD band definition v3.1, and is therefore not produced.

1.5 Getting access to the data

Interested users can get access to the data via the EUMETSAT UMARF, the unified meteorological archive facility. The procedure involves a registration and after this step the user can select and request the data. For more information please consult the "Access to Data" section on the EUMETSAT website, or go directly to the UMARF archive via the following URL:

http://archive.eumetsat.int/umarf/

1.6 Abbreviations and acronyms

AAI Absorbing Aerosol Index
AAH Absorbing Aerosol Height
ATBD Algorithm Theoretical Basis Document
BBA Biomass Burning Aerosols

BRDF	Bidirectional Reflectance Distribution Function
BSA	Black-Sky Albedo
CDOP	Continuous Development & Operations Phase
DAK	Doubling-Adding KNMI
DDA	Desert Dust Aerosols
DOAS	Differential Optical Absorption Spectroscopy
DU	Dobson Units, 2.69×10^{16} molecules cm^{-2}
EUMETSAT	European Organisation for the Exploitation of Meteorological Satellites
ENVISAT	Environmental Satellite
ERS	European Remote Sensing Satellite
ESA	European Space Agency
FRESCO	Fast Retrieval Scheme for Cloud Observables
GOME	Global Ozone Monitoring Experiment
HDF	Hierarchical Data Format
IT	Integration Time
KNMI	Koninklijk Nederlands Meteorologisch Instituut (De Bilt, NL)
LER	Lambertian-Equivalent Reflectivity
LUT	Look-Up Table
MERIS	Medium Resolution Imaging Spectrometer
MLS	Mid-Latitude Summer
MSC	Main Science Channel
NISE	Near-real-time Ice and Snow Extent
NRT	Near-Real-Time
OMI	Ozone Monitoring Instrument
O3M SAF	Satellite Application Facility on Ozone and Atmospheric Chemistry Monitoring
PMD	Polarisation Measurement Device
PSD	Product Specification Document
PUM	Product User Manual
RTM	Radiative Transfer Model
SCIAMACHY	Scanning Imaging Absorption Spectrometer for Atmospheric Chartography
SZA	Solar Zenith Angle
TEMIS	Tropospheric Emission Monitoring Internet Service
TOA	Top-of-Atmosphere
TOMS	Total Ozone Mapping Spectrometer
UTC	Universal Time Co-ordinate
UV	Ultra-Violet
VIS	Visible
VZA	Viewing Zenith Angle

2 Instrument degradation

2.1 Introduction

Instrument degradation is a serious problem which strongly affects the Earth reflectance measurements performed by GOME-2 in the UV wavelength range [*Tilstra et al.*, 2012b]. As a result, it also has an impact on the AAI products retrieved from the GOME-2 instruments [*Tilstra et al.*, 2010]. For this reason, we apply correction factors to the Earth reflectances that are found in the GOME-2 level-1b product. The method that we use to derive these in-flight degradation correction factors has been introduced earlier in *Tilstra et al.* [2012a] for the SCIAMACHY instrument. The method was later successfully applied to correct the GOME-2 instruments [*Tilstra et al.*, 2012b].

2.2 Measuring instrument degradation

The method is based on studying time series of the daily global mean reflectance. The daily global mean reflectance, denoted by $R^\star$, is defined as the mean of all measured Earth reflectances for a certain scan mirror position on a certain day between 60°N and 60°S and solar zenith angles θ_0 less than 85 degrees. In Figure 1 we present two plots taken from *Tilstra et al.* [2012b] which show the daily global mean reflectance as a function of time for the GOME-2 instrument.

The time series of the global mean reflectance show seasonal variations as well as trends due to instrument degradation. To analyse the time series, we assume that the global mean reflectance may be well described empirically by a function made up of a polynomial term, representing the reflectance change due to instrument degradation, multiplied by a term periodic in time that represents the normal seasonal variation of the global mean reflectance. In other words,

$$R^\star_{\lambda,s} = P^{(p)}_{\lambda,s} \cdot [1 + F^{(q)}_{\lambda,s}] \,, \tag{1}$$

where the term P represents the polynomial part of degree p, defined by

$$P^{(p)}_{\lambda,s}(t) = \sum_{m=0}^{p} u^{(m)}_{\lambda,s} \cdot t^m \,, \tag{2}$$

while the seasonal variation F is described by a finite Fourier series of order q, according to

$$F^{(q)}_{\lambda,s}(t) = \sum_{n=1}^{q} [v^{(n)}_{\lambda,s} \cdot \cos(2\pi n t) + w^{(n)}_{\lambda,s} \cdot \sin(2\pi n t)] \,. \tag{3}$$

In these equations, the parameter t is the time expressed in years since the beginning of the time series (which is 4 January 2007 in the case of GOME-2 on MetOp-A). The parameter λ refers to the wavelength and the integer s relates to the scan mirror position. For GOME-2, this integer runs from

1 to 32 for the nominal integration time (IT) of 187.5 ms when the instrument scans from east to west and back. For the present baseline, we use $p = 4$ and $q = 6$ for GOME-2 on MetOp-A.

The polynomial part P is the most important as it represents the relative change in the GOME-2 measured Earth reflectance over the years, per scan mirror position, due to instrument degradation. Normalisation of P immediately leads to the reflectance degradation factor:

$$d_{\lambda,s}(t) = P^{(p)}_{\lambda,s}(t) \,/\, P^{(p)}_{\lambda,s}(0) \,. \tag{4}$$

For GOME-2 the reflectance degradation factor is growing with time for most wavelengths, and it is strongly dependent on scan mirror position. Figure 1 shows the behaviour for 340 and 380 nm.

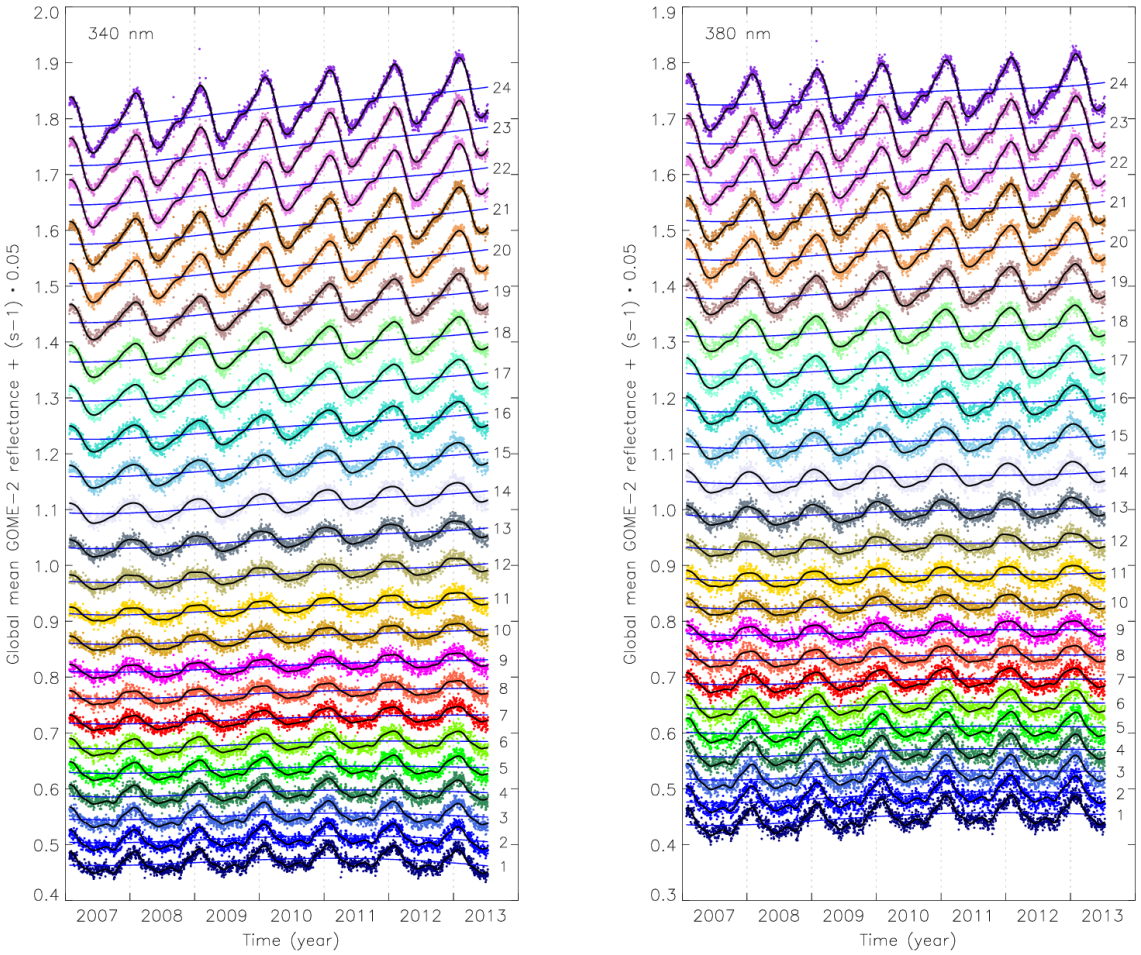

Figure 1: Global mean reflectance measured by GOME-2 at 340 nm (left) and 380 nm (right) as a function of time, for each of the 24 scan mirror positions in the forward scan. To separate the time series graphically, an offset of $(s-1)\cdot 0.05$ *was added to each, where* s *is the scan mirror position as indicated. The solid black curves are fit results and are described in the main text. The blue monotonous curves illustrate the effect of instrument degradation over the years.*

2.3 Correcting instrument degradation

The correction for instrument degradation can easily be calculated using

$$c_{\lambda,s}(t) \equiv 1/d_{\lambda,s}(t) = P^{(p)}_{\lambda,s}(0) \,/\, P^{(p)}_{\lambda,s}(t) \,. \tag{5}$$

The measured Earth reflectances have to be multiplied with these correction factors. In the operational processing chain, these correction factors are determined daily, by calculating the global mean reflectances at 340 and 380 nm for the previous day, and appending the result to the historical archive of global mean reflectances. After that, the method outlined in section 2.2 is executed, which provides a forecast for the present day. Each day this procedure is repeated, yielding up-to-date full mission correction factors. The results can be monitored via the following URL:

http://www.temis.nl/o3msaf/globalmean.php

The time series of global mean reflectance and corrections factors have to be calculated for each instrument, and for main science channel and PMD bands separately.

2.4 Impact of instrument degradation on the AAI

As an example of the impact of instrument degradation, we present in Figure 2 time series of the *uncorrected* global mean residue as a function of time, for each of the 24 scan mirror positions in the forward scan of the instrument. The *uncorrected* AAI is available in the AAI product under field name "UncorrectedResidue". Note that these data should never be used. They are available in the product for the purpose of monitoring the impact of instrument degradation. The *corrected* AAI data are stored under field name "AAI". These are the data to be used by the users of the AAI products, and these are the data that will be discussed in the remaining part of this validation report.

As can be concluded from Figure 2, the impact of instrument degradation on the AAI is indeed very large. The instrument degradation is depending on the scan mirror position. For instance, at the westernmost position in the orbit swath (IndexInScan = 24), the global mean residue is currently almost 3 index points lower than at the start of the GOME-2 mission. At the easternmost position in the orbit swath (IndexInScan = 1), the global mean residue has increased by almost 1.5 index points.

Several vertical lines in Figure 2 indicate notable events in the MetOp-A life time. Jumps in the global mean residue can occur at the dates associated with these lines. One vertical line corresponds to 11 March 2008. On this day, a new PMD band definition (v3.1) was uploaded to the satellite instrument. As a result, the global mean residue jumped up by $\sim$0.2 index points. Another vertical line corresponds to 9 September 2009, right in the middle of a throughput test of the GOME-2 instrument. The direct effect of this throughput test was very small. A third vertical line corresponds

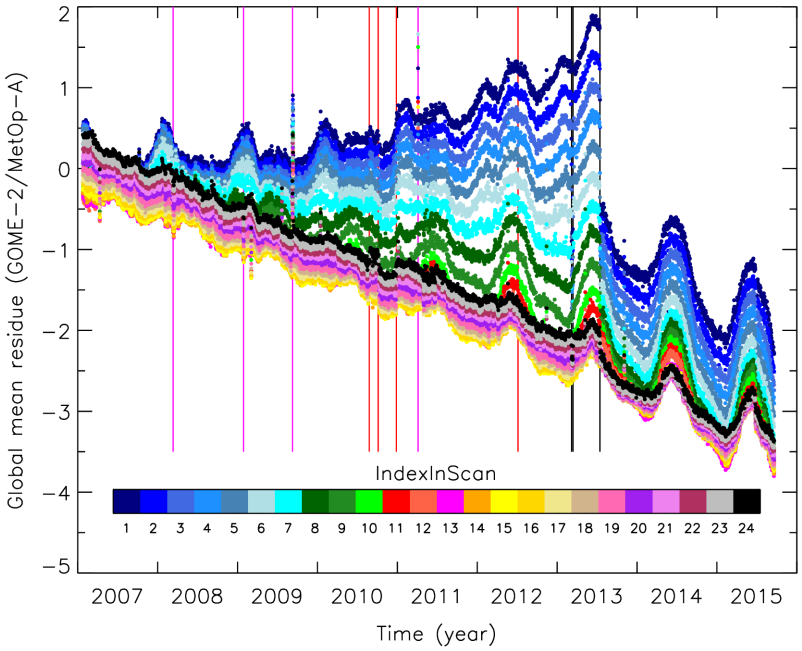

Figure 2: Daily global mean residue observed by GOME-2 on MetOp-A versus the time for all 24 forward scan mirror positions inside the GOME-2 swath. The colour bar links the colours to the "IndexInScan" number. The trend due to instrument degradation varies with scanner angle.

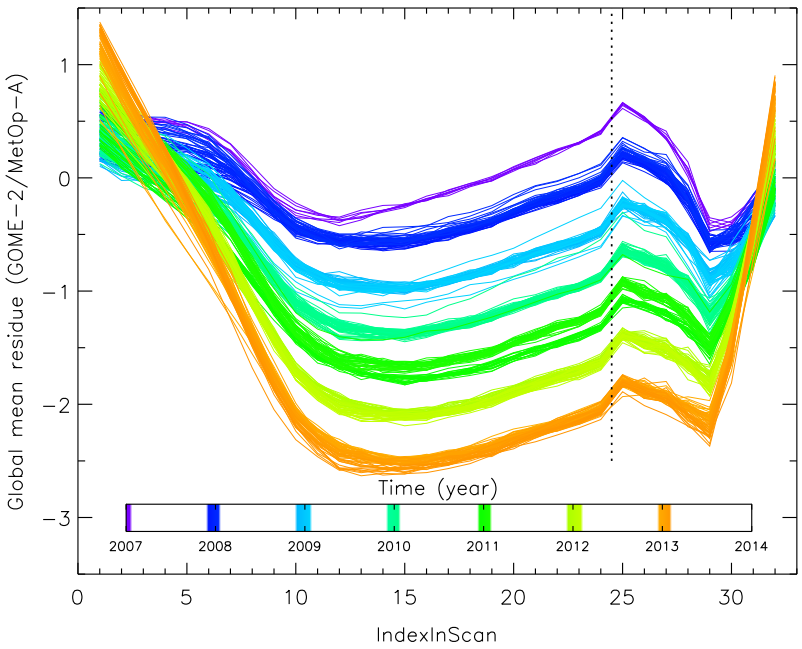

Figure 3: Global mean residue as a function of scanner mirror position, for all available days in the months December and January of the years up to 2013. The colours can be related to the actual date using the colour bar. The vertical dotted line illustrates the westernmost scanner angle position.

to the swath width reduction that took place on 15 July 2013. Other vertical lines are related to changes in the (level-1) processor. These events are all not related to instrument degradation and are therefore not affected, corrected or treated in any way by the algorithm.

In Figure 3 we present the same data but in a different way. We plot the dependence of the global mean residue on scanner angle for all days in the months December and January. The figure clearly demonstrates the dependence of the global mean residue on the scan mirror angle (i.e., on the scattering geometry), and the change in this dependence due to the impact of instrument degradation.

2.5 Accuracy

The correction method that we use was estimated to be accurate within 0.2% [*Tilstra et al.*, 2012a]. That is, a trend in the Earth reflectance is removed to within the percent level. Using the rule of thumb that a one percent change in reflectance leads to a residue change of half an index point, we estimate that the accuracy of the correction for instrument degradation is better than 0.2 index points over the entire time range covered by the GOME-2 instruments.

3 SCIAMACHY versus GOME-2

3.1 Short introduction

In this section we present validation results from a direct comparison between (i) the AAI measured by GOME-2 on MetOp-A, and (ii) the AAI measured by SCIAMACHY on Envisat (at roughly the same time and place). Because of the slightly different orbital periods, such an intercomparison is not possible for all days of the year. However, for many days on which intercomparison is possible, the orbit tracks overlap completely, ensuring that the scattering geometries (i.e., viewing and solar angles) are nearly identical, which adds to credibility and reliability of the intercomparison.

3.2 Description of SCIAMACHY

SCIAMACHY (Scanning Imaging Absorption Spectrometer for Atmospheric Chartography) [*Bovensmann et al.*, 1999] was launched on 1 March 2002 onboard the Envisat satellite into a near-polar, sun-synchronous orbit, with an orbital period of about 101 minutes, comparable to the MetOp-A orbit. The local crossing time of the equator is 10:00 a.m., so SCIAMACHY observes a certain ground scene 30 minutes after GOME-2 does. A major difference with respect to GOME-2 is that SCIAMACHY has the ability to perform not only nadir measurements, but also limb measurements. These two measurement modes are being alternated along the orbit. The resulting data are stored in blocks, called "states". A nadir state covers an area of 960×490 km^2 (across track $\times$ along track).

The wavelength region covered by SCIAMACHY is 240–2380 nm, with a spectral resolution of 0.2–1.5 nm. The scanning sequence is similar to that of GOME-2: 4 s forward scan and a fast reverse scan in 1 s. The swath is 960 km wide, half of that of GOME-2. Another major difference with GOME-2 is that the nadir spectrum is divided into 56 wavelength regions, called "clusters", that are all read out with their own integration time (IT). This allows a higher spatial resolution for the most important spectral regions, at the expense of other wavelength regions where the spectrum is of less scientific interest, or would otherwise yield a weak signal. Typical ITs are 0.25 s (pixel size 60×30 km^2) and 0.5 s (pixel size 120×30 km^2). Owing to the alternation of nadir and limb modes, global coverage in nadir is achieved in only 6 days instead of the 1.5 days for the GOME-2 instrument.

3.3 Intercomparison approach

Figure 4 explains the approach that was followed in a graphical way. For a given day, in this case 17 October 2007, we gather all SCIAMACHY and GOME-2 AAI orbits that are available to us. For each SCIAMACHY orbit, we determine, in an intelligent way, the equator passing point (EPP). Using this

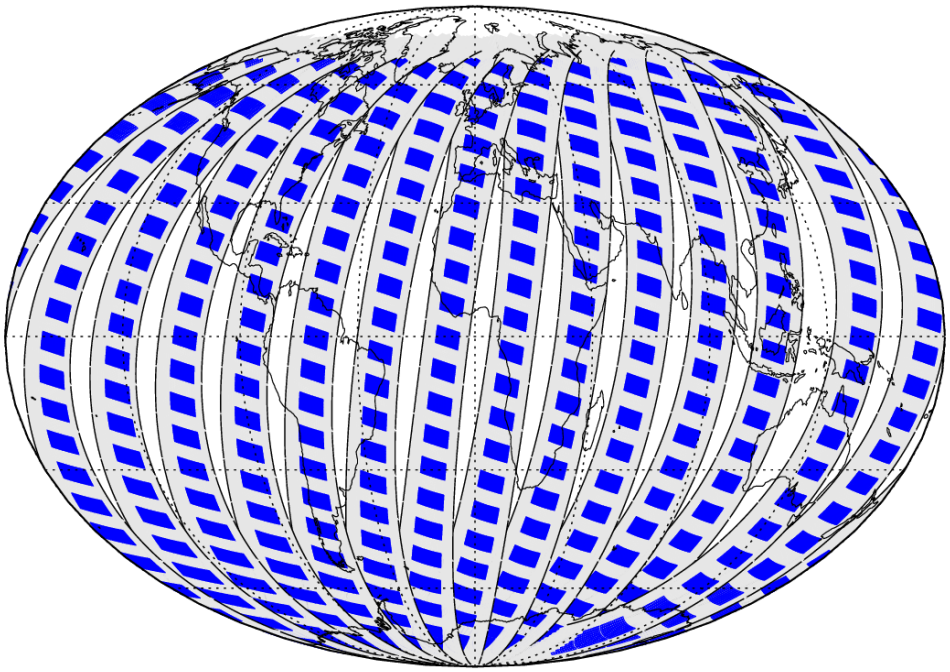

Figure 4: Graphical explanation of the approach that was followed to compare the GOME-2 AAI's with those determined by SCIAMACHY. The black curves indicate the GOME-2 swaths borders. The blue boxes indicate the individual SCIAMACHY footprints. The data are from 17 October 2007.

information, we look for the GOME-2 orbit that has a more or less identical EPP. If this orbit exists, then we have a match. Note that, because of the different equator passing times (GOME-2: 09:30 LT; SCIAMACHY: 10:00 LT), there is a 30-minutes time difference. Related to this, there is also a slight difference in the solar zenith angle (SZA) which goes up to 7 degrees near the equator.

After that, we concentrate on all SCIAMACHY forward scan pixels between 70°N and 70°S that have a SZA below 80°. For all the pixels in this subset, we start looking for the GOME-2 forward scan pixels that belong to it, record their residues, and take the mean if more than one are found. The result we will call the "collocated GOME-2 AAI" from now on. We can then analyse the results, as shown in Figure 5. Here we plotted the collocated GOME-2 AAI versus the original SCIAMACHY AAI. The version of the SCIAMACHY AAI data is the latest version 5.1, which was released on 7 June 2012. The agreement is rather good, although there is quite some scatter around the expected one-to-one relationship. This scatter can be explained in a number of ways.

First of all, we have a 30-minutes time difference between SCIAMACHY and GOME-2, which could lead to a change in the observed scene in the case of clouds. Note that the largest scatter occurs at negative values, i.e., in the regime of cloudy scenes. By filtering out cloudy scenes we could indeed reduce the scatter a bit, of course at the expense of the number of available data points. Secondly, there is a difference in the solar zenith and azimuth angles of SCIAMACHY and GOME-2. Thirdly,

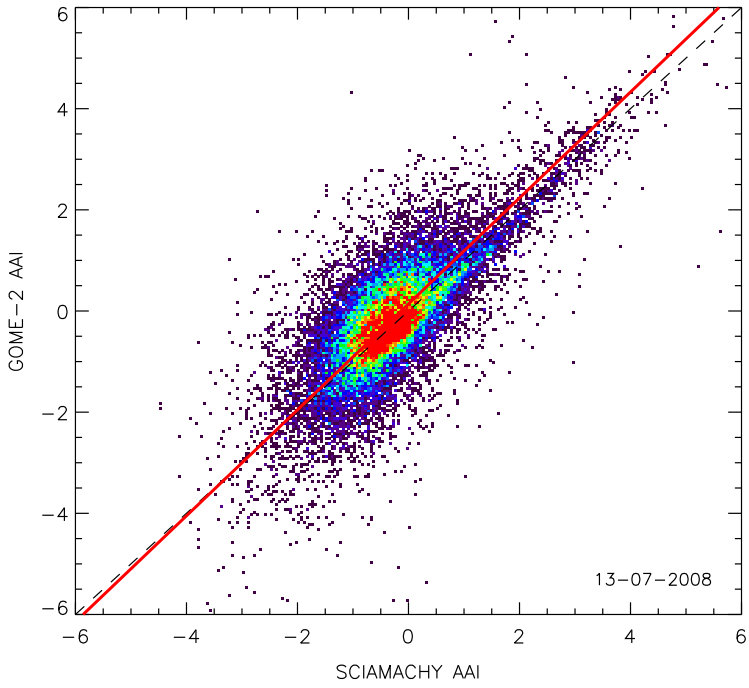

Figure 5: The "collocated GOME-2 AAI" versus the SCIAMACHY AAI, for 13 July 2008. The agreement is fair, considering the fact that we took no effort to improve handling the spatial mismatch between the SCIAMACHY and GOME-2 footprints. The red line is a linear fit to the data points.

and most importantly, the SCIAMACHY and GOME-2 footprints do not overlap completely, so there will always be a spatial collocation mismatch between the SCIAMACHY and GOME-2 footprints. We took no action to improve on this, because the goal is to analyse the entire collection of data as a whole, not to improve the intercomparison of individual ground pixels.

In Figure 5 we also present a red line, which is a linear fit to the data points. Weighted fitting was not applied, but residues with values lower than -10 and higher than $+10$ were not trusted and were therefore not allowed to take part in the fitting process. For the specific day shown in Figure 5, 13 July 2008, the slope was found to be 1.04 ± 0.06 and the intercept was 0.16 ± 0.05, pointing to good agreement between the GOME-2 and SCIAMACHY AAI. Note that the SCIAMACHY AAI was found to be well calibrated w.r.t. GOME-2's predecessor GOME-1 [*Tilstra et al.*, 2007, 2011].

3.4 Results

The analysis described in the previous section was performed on the entire GOME-2 AAI reprocessed data set that was available. This data set covers most of the period 2007–2013. While processing the data set, we recorded the number of orbits for which we could successfully link the SCIAMACHY data to GOME-2 data. When a SCIAMACHY monitoring orbit was encountered (narrow swath, nadir

static, et cetera), then this orbit was skipped altogether. When a GOME-2 narrow swath or nadir static orbit was encountered, this orbit was not skipped, but it was recorded that a narrow swath/nadir static orbit was used that day. We decided to remove days with more than two of such orbits.

Because of the slightly different orbital periods of SCIAMACHY and GOME-2, in general the orbit tracks of the two instruments do not overlap. Every nine days, however, the situation occurs that they do overlap, for a relatively short period of $\sim$2 days (depending on how strict we are). For each day for which we could find SCIAMACHY and GOME-2 orbits with overlapping orbit tracks, we recorded the number of these orbits. Slope and intercept of the linear fit to the collocated AAI's, performed in the way described before, were also recorded. Figure 6 presents the resulting slopes as a function of time. The red circles are results which are not reliable, either because there were not enough orbit track overlaps found (say, less than 10), or because there were two or more narrow swath/nadir static orbits involved. The blue circles are the remaining results, which we expect to be reliable.

As can be seen, the red circles are scattered, but the blue circles are much more consistent in their behaviour. At first sight, there appears to be a good correlation between the SCIAMACHY and GOME-2 residues, with slopes in general close to one. On the other hand, there seems to be a periodic or seasonal variation hidden behind the scatter in the slopes. In Figure 7, we plotted the intercepts of the linear fits. The offset found is small and partially hidden by the noise in the data points. There does not appears to be a trend present in the time series. Such a trend, if it would exist, could be related to changes in the radiometric calibration of GOME-2, for instance due to instrument degradation. The absence of such a trend in Figure 7 therefore adds to the credibility of the correction for instrument degradation that was presented in section 2. Note that a one index point offset can already be explained by a 2% error in the reflectance [*Tilstra et al.*, 2012a].

As for the time dependence of the slopes and intercepts shown in Figures 6 and 7, we have to conclude that – at least within the accuracy of the intercomparison – no clear systematic time dependence was found. This is expected for the slopes, because radiometric calibration errors only slightly affect the slopes, while strongly affecting the intercepts. The intercepts also show no clear time dependence. This indicates that the GOME-2 AAI has been stable over the years covered by the time series.

3.5 Results – Improving the intercomparison (method B)

The statistical errors on slope and intercept, determined in the linear fitting process as illustrated in Figure 5, are both on the order of 0.05. This is much less than the large variability that is actually found in Figures 6 and 7. The much larger error is caused by a systematic error, namely the unavoidable longitudinal misalignment between the SCIAMACHY and GOME-2 orbits. Figure 4 explains this more clearly. For the day in question, 17 October 2007, the first SCIAMACHY and GOME-2 orbits have near perfect overlap, but at the end of the day, the overlap is already quite poor. For the

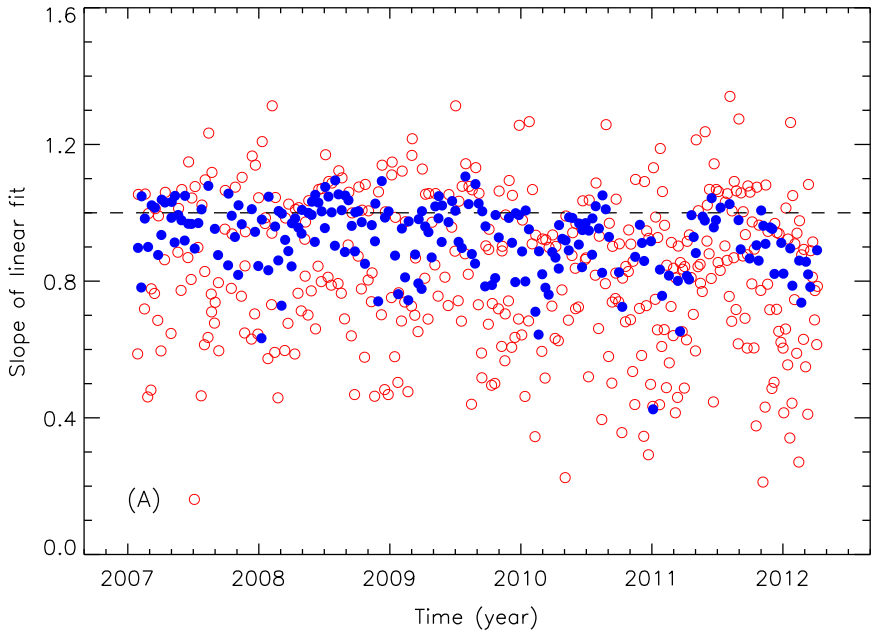

Figure 6: Slope of the linear fits to the (GOME-2 versus SCIAMACHY) data points as a function of time. The red circles are unreliable: not enough orbits with perfect orbit track overlap between SCIAMACHY and GOME-2, and/or too many GOME-2 narrow swath orbits included. The blue circles are believed to be reliable, although some scatter is obviously present in the blue data points.

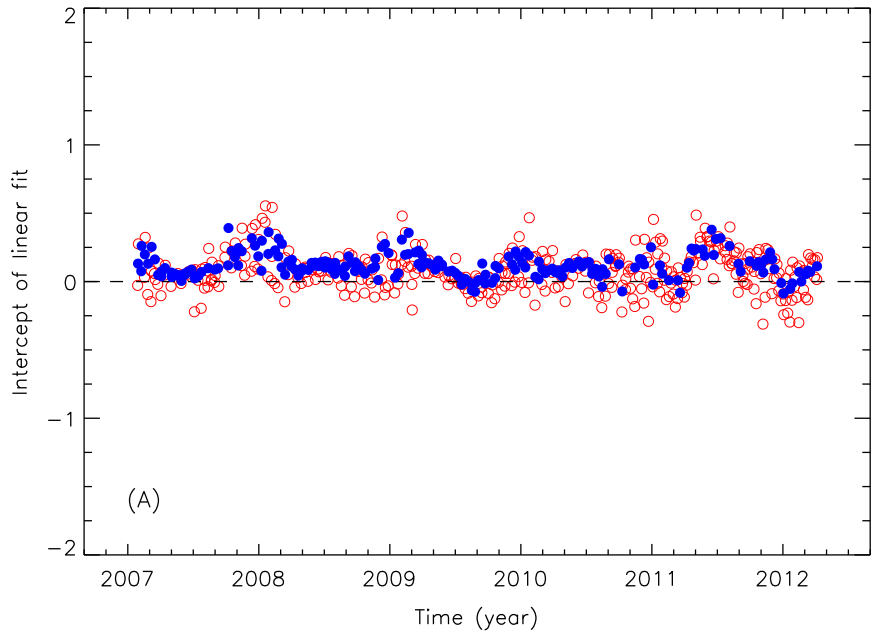

Figure 7: Intercept of the linear fit. The colour coding and its meaning are the same as in Figure 6. The result shows that there is no clear offset found over the studied time period.

previous day, i.e., 16 October 2007, the situation is exactly the other way around. The best thing to do in this particular case would be to take the last ∼7 orbits of 16 October 2007, and the first ∼7 orbits of 17 October 2007, and to glue these together to form an artificial "new day". The resulting collection of orbits of this "new day" would have a much better average longitudinal alignment than the collection of orbits of the two original, individual days.

We therefore abandon the idea of letting each day start at 00:00:00 UTC and instead determine a careful selection of subsequent orbits for which the longitudinal misalignment, in the absolute sense, is below a certain threshold. The threshold used was 1.6 degrees in longitude which in normal situations yields between 14 and 17 contiguous orbits that fulfil this criterion. The artificial days created this way cover a time period of roughly 24 hours, i.e., the selected orbits are spread out over the entire longitude range of the globe. Figure 8 shows the relative longitudinal alignment for a selection of associated SCIAMACHY and GOME-2 orbits taken from 26 and 27 February 2007. All selected orbits have an absolute relative longitudinal alignment less than 1.6 degrees.

In Figure 9 we present again a time series of the slope of the linear fit to the data points in the scatter plots, but now for the artificial "new days". We will call this new approach "method B" from now on. As before, the red circles indicate days for which not enough orbits were available. Compare with Figure 6. Clearly, the variability in the slopes has been reduced enormously. It now amounts to roughly 0.01–0.03, which relates well to the statistical errors reported by the fitting processes. This confirms that we have removed an important error source using the new method "B".

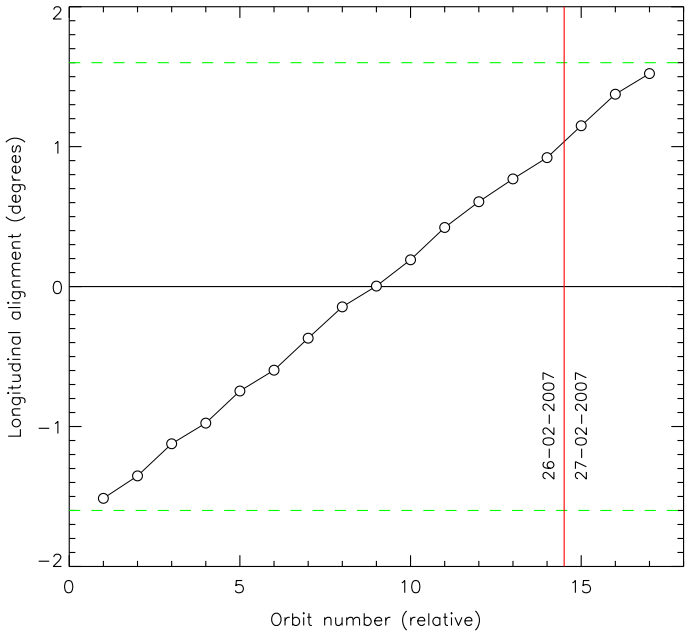

Figure 8: Longitudinal alignment for a selection of overlapping SCIAMACHY and GOME-2 orbits from 26 and 27 February 2007. All orbits have a longitudinal misalignment less than 1.6 degrees.

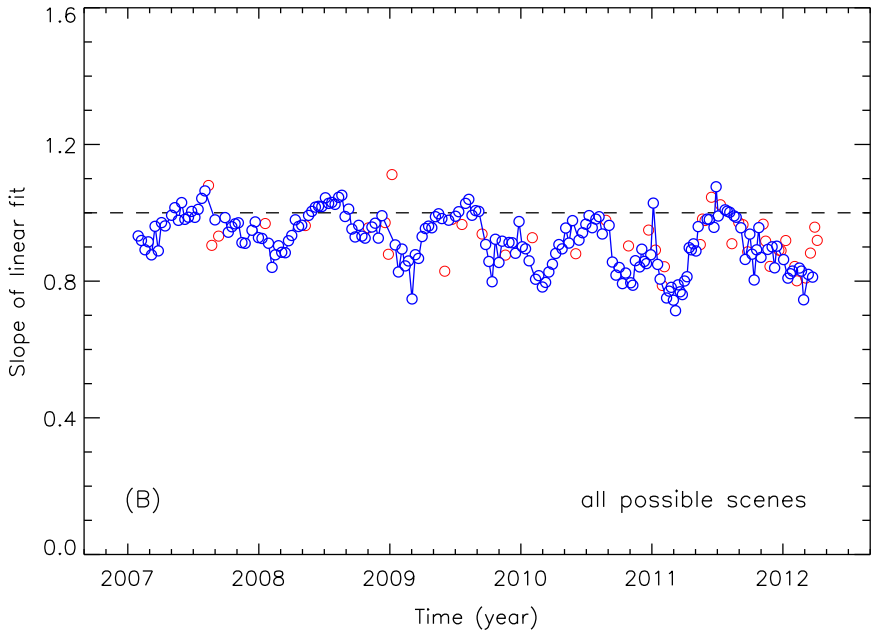

Figure 9: Slope of the linear fits to the (GOME-2 versus SCIAMACHY) data points as a function of time, for the new approach in which artificial days are created (method "B", see text). The red circles are less reliable: not enough orbits and/or too many GOME-2 narrow swath orbits.

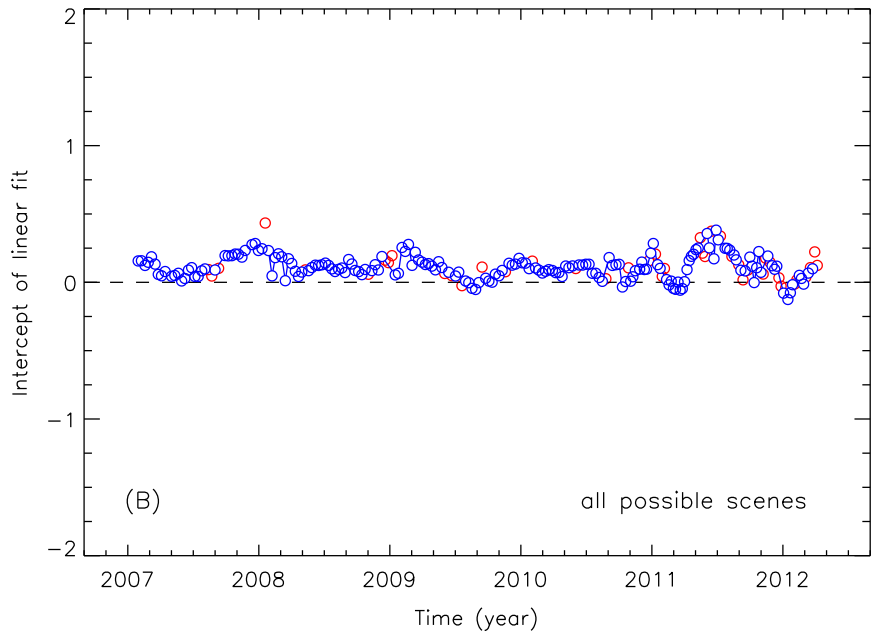

Figure 10: Intercept of the linear fit, for the new approach "B" in which artificial days are created. The colour coding and meaning is the same as in Figure 9. We conclude that there is only a very small offset of the GOME-2 AAI w.r.t. the SCIAMACHY AAI, on the order of 0.1–0.2 index points.

The improved accuracy, and the resulting reduced variability, now reveal that there is a seasonal variation found in the SCIAMACHY versus GOME-2 intercomparison, at least for the slope of the linear fit. The existence of a seasonal variation in the slope is not understood, and will be examined more closely in the next section. In Figure 10 we present a time series of the intercept of the linear fit to the data points in the scatter plots. The variability has been reduced considerably.

Figure 11 presents the standard deviation σ of the GOME-2 versus SCIAMACHY data points in relation to the achieved linear fit. That is, if the GOME-2 AAI's are represented by the array y_i, and the SCIAMACHY AAI's are represented by the array x_i, and the best linear fit to the data can be represented by $y = mx + n$, where m is the slope and n is the intercept of the linear fit, then the standard deviation is defined as $\sigma(y_i - mx_i - n)$. The standard deviation is on the order of 0.5 index points. Note that this means that the (bias-corrected) GOME-2 AAI is therefore shown to be validated against the SCIAMACHY AAI within an accuracy $\sim$0.5 index points. Also note that, although we went through a great deal of trouble to achieve an as accurate as possible intercomparison, there is still an inaccuracy to be attributed to the intercomparison procedure itself. That is, the "real" (intrinsic) uncertainty in the GOME-2 AAI will be less than the standard deviation of $\sim$0.5 index points reported here, because the standard deviation also includes inaccuracies introduced by the intercomparison approach itself.

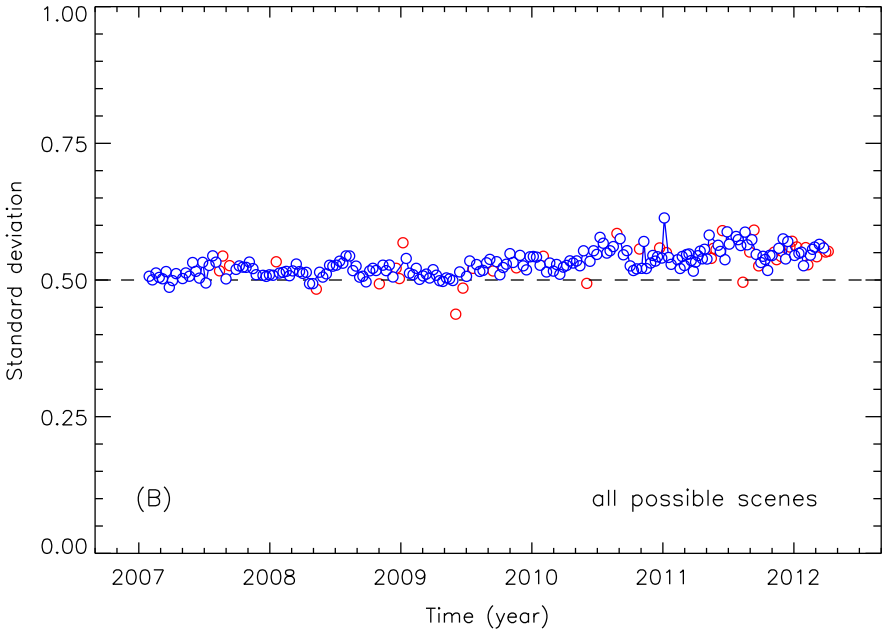

Figure 11: Standard deviation of the difference between linear fit and the data, for the new approach "B" in which artificial days are created. The standard deviation is roughly 0.5 index points, showing a slight increase with time. As before, the results for the red circles are believed to be unreliable.

3.6 Scene dependencies

In this section we will perform a re-analysis of the results, this time distinguishing between different scene types. This is necessary, because the results of the previous sections showed indications of the presence of a seasonal variation in the time series. The presented slopes oscillated mildly below the expected one-to-one relationship. We have to exclude the possibility that the low aerosols loadings in the months October to December, resulting in an absence of data with positive residues, affect the linear fit a negative way, thereby possibly creating a synthetic seasonal dependence in the time series. In our analyses, we distinguish the following three scene types:

1. cloudy scenes: SCIAMACHY FRESCO cloud fraction ≥ 0.1

2. clear sky scenes: SCIAMACHY FRESCO cloud fraction < 0.1 and SCIAMACHY residue < 0.5

3. aerosol loaded scenes: SCIAMACHY residue ≥ 0

The resulting time series of slope and intercept of the linear fits to the GOME-2 versus SCIAMACHY data points are shown in Figures 12–17. Both the slope and intercept found for the subset of cloudy scenes turns out to be similar to the overall case shown in Figures 9 and 10, where all scenes were taken into account. This is perfectly understandable, as most of the observations are in fact cloud contaminated, and cloudy scenes therefore determine the overall case. To give an indication of the number of scenes that are typically involved, the number of cloudy, clear sky, and aerosol loaded scenes for the "new day" of 26/27 February 2007 (see section 3.5) was 19384, 6976, and 7332, respectively, compared to the total number of 31335 scenes.

The slopes found for the clear sky cases show no clear seasonal variation, and are more or less equal to one. Note that the retrieved intercepts are about 0.3 index points lower than the intercepts found for the cloudy cases. The slopes of the aerosol loaded cases show a large scatter, due to the low number of aerosol loaded scenes and the small residue range on which to we have to perform the fit. A seasonal variation might or might not be present, it is impossible to judge from the results presented in Figure 16. The time series of the intercept shows a lot less scatter.

To be able to study the behaviour of the aerosol loaded scenes we gather all SCIAMACHY and GOME-2 AAI measurements of the years 2007 and 2008 found using the approach described in section 3.5 (method "B"). Figure 18 presents the scatter plot of GOME-2 versus SCIAMACHY of these AAI data. The biases found in Figure 10 were subtracted from the GOME-2 AAI measurements, so the GOME-2 AAI's are by definition bias-corrected w.r.t. the SCIAMACHY AAI's. Note that all scenes are contained in the scatter plot, not just aerosol loaded scenes. The blue curve is a linear fit to all the data, with slope 0.97 ± 0.05. The red curve, on the other hand, is a fit to the subset of

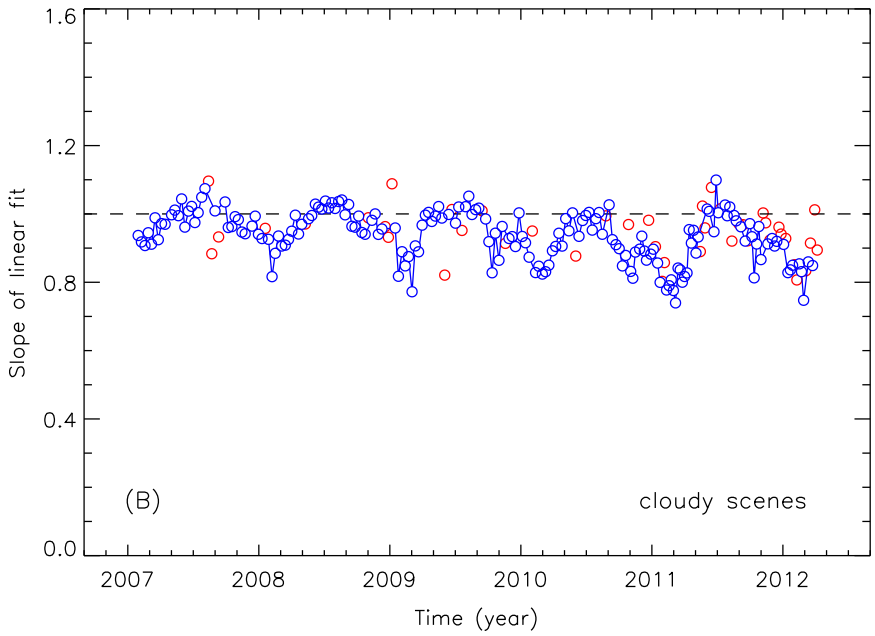

Figure 12: Slope of the linear fit for cloudy scenes, according to the validation method described in section 3.5. The SCIAMACHY FRESCO cloud fraction was larger than 0.1 for all measurements.

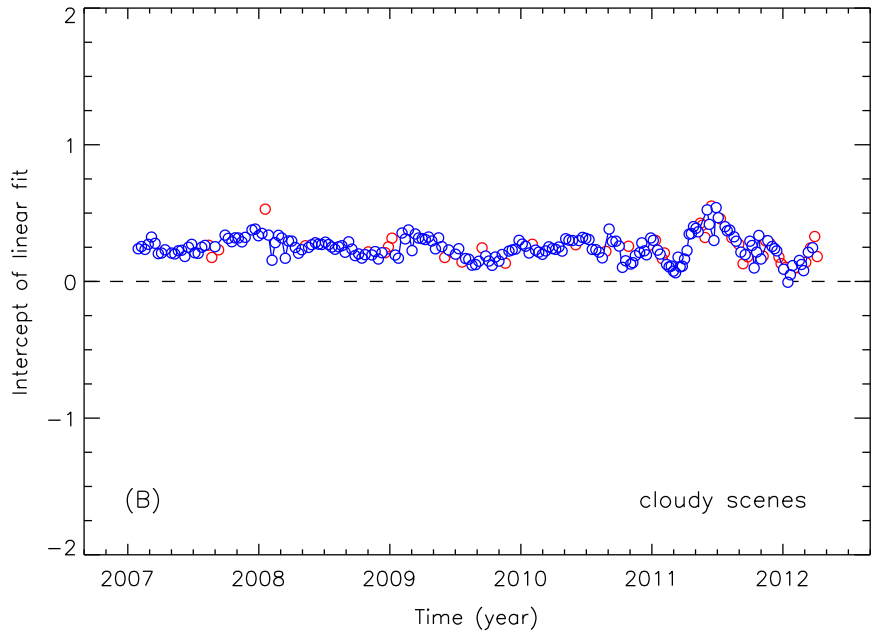

Figure 13: Intercept of the linear fit for cloudy scenes, according to the validation method described in section 3.5. The SCIAMACHY FRESCO cloud fraction was larger than 0.1 for all measurements.

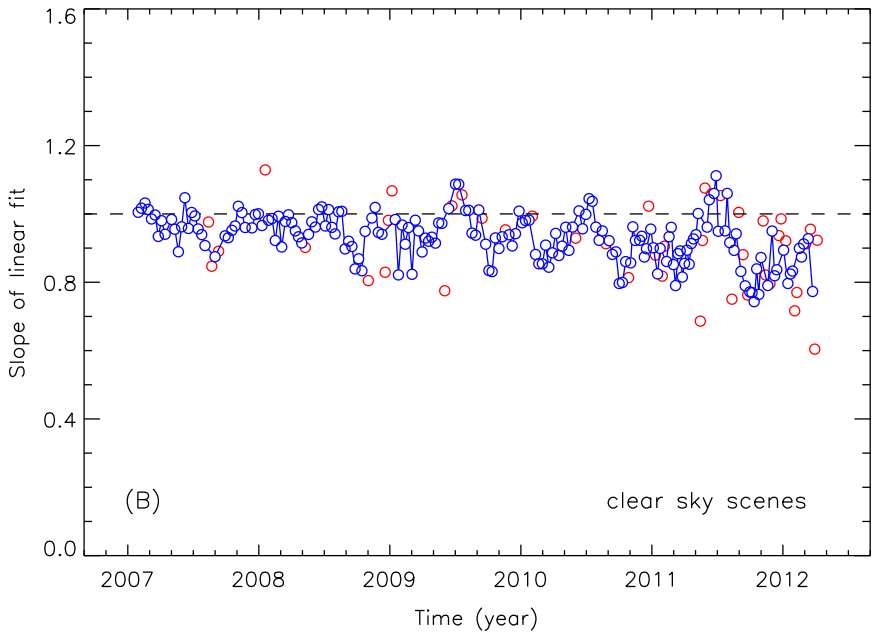

Figure 14: Slope of the linear fit for clear sky scenes, according to the validation method described in section 3.5. FRESCO cloud fraction smaller than 0.1 and SCIAMACHY AAI smaller than 0.5.

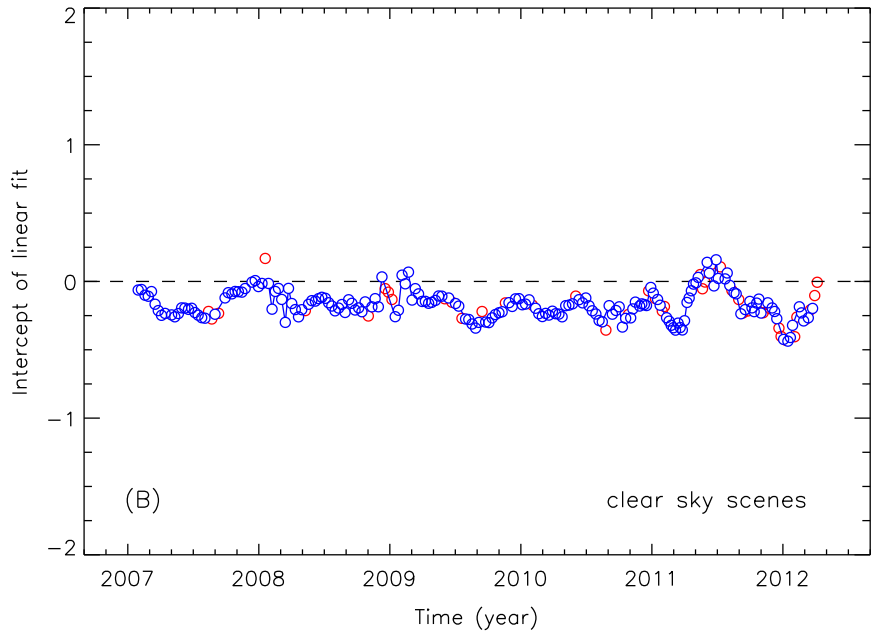

Figure 15: Intercept of the linear fit for clear sky scenes, according to the validation method described in section 3.5. FRESCO cloud fraction smaller than 0.1 and SCIAMACHY AAI smaller than 0.5.

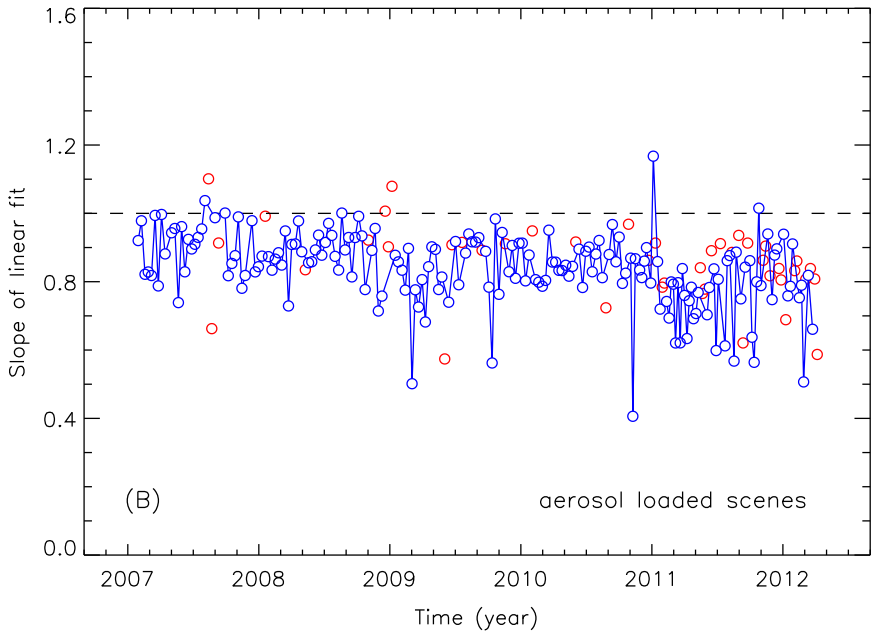

Figure 16: Slope of the linear fit for scenes with a sizeable aerosol load (SCIAMACHY AAI larger than 0.5). The large scatter in the data points is caused by the small number of data points having a positive residue. This is especially the case outside the aerosol season.

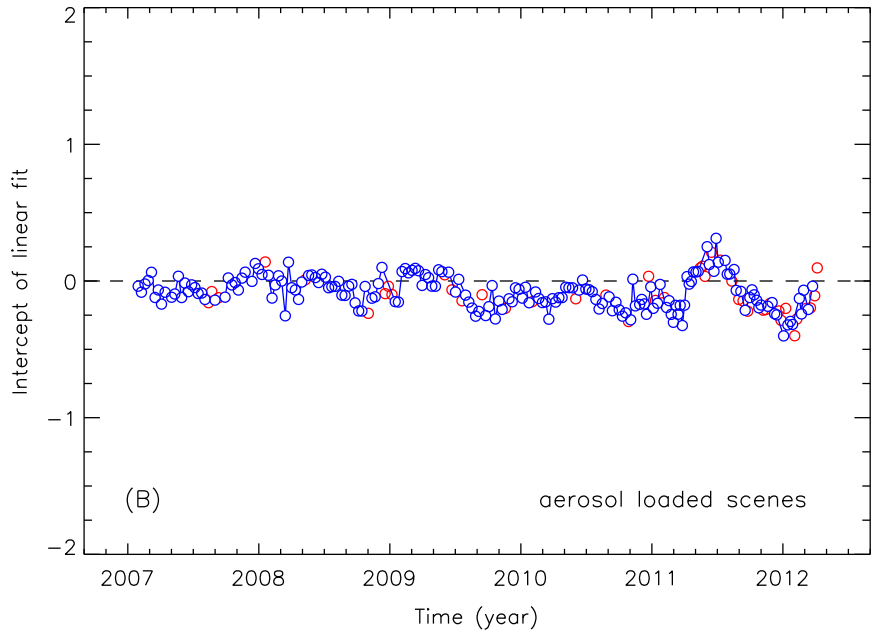

Figure 17: Intercept of the linear fit for scenes with a sizeable aerosol load. The SCIAMACHY AAI was larger than 0.5 for all measurements used.

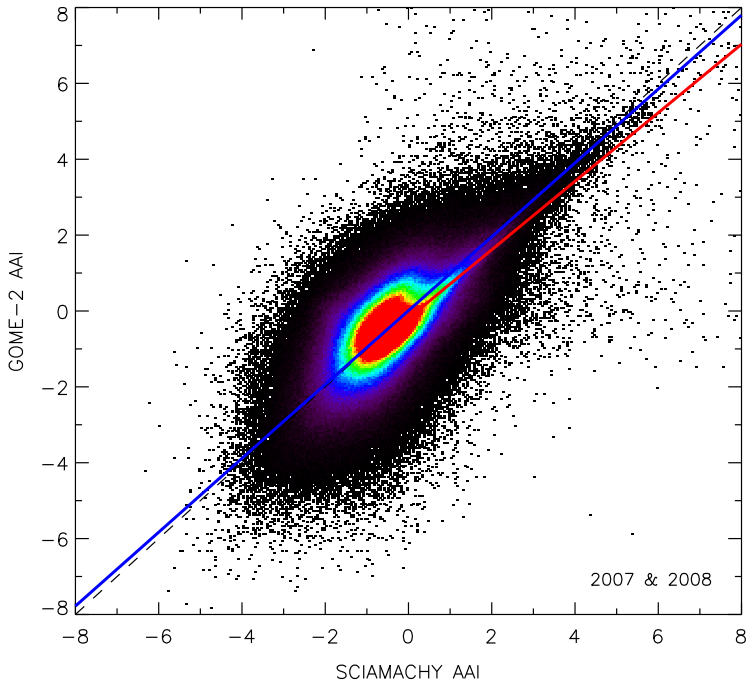

Figure 18: The collocated GOME-2 AAI versus the SCIAMACHY AAI, taken from all the 72 artificial days found in 2007 and 2008 for which the collocation is nearly perfect. The GOME-2 AAI's were bias-corrected. The blue curve is a linear fit to the data, with slope 0.97 ± 0.05*. The red curve is a fit to the subset of measurements of aerosol loaded scenes. The slope is* 0.90 ± 0.01*.*

measurements of aerosol loaded scenes (that is, SCIAMACHY AAI > 0). The slope in this cases is 0.90 ± 0.01, close to one. This proves that, averaged over two years, there is indeed a near one-to-one relationship found between the SCIAMACHY and GOME-2 AAI for aerosol loaded scenes.

In conclusion, we found a seasonal variation in the GOME-2 versus SCIAMACHY intercomparison results. It is possible that the seasonal variation is real, i.e., really present in the GOME-2 AAI data. But it could also be artificial, i.e., an artefact of the intercomparison itself. Possibly the seasonal variation is caused by the seasonal variation in global aerosol loads which could affect the fitting results. The results of this section, however, do not provide a clear proof for this. At the same time, the intercomparison might also be affected by the fact that the SCIAMACHY and GOME-2 measurements have slightly different solar zenith angles (see section 3.3). This could lead to a seasonal variation having the right period and phase. This all remains speculation at this point, however.

Supposing that the seasonal variation that we found is real, then it would most likely a radiometric calibration problem because the algorithm of the SCIAMACHY AAI is very similar to the algorithm of the GOME-2 AAI. This has been checked thoroughly in the past. Note that we cannot fully exclude the possibility that SCIAMACHY causes the seasonal variation, although we should also point out that this instrument has been found to be well-calibrated w.r.t. GOME-1. At this point we

have to accept that we cannot find out if the seasonal variation is "real" or "artificial". Note that the magnitude of the seasonal variation is very small to begin with. Its presence does not prevent us from concluding that the GOME-2 AAI is well calibrated w.r.t. the SCIAMACHY AAI.

3.7 Discussion of results

The results seem to indicate that there is a good correlation between the GOME-2 AAI and the SCIAMACHY AAI that was used as a reference. The correlation is good in the sense that (i) there is a clear linear relationship between the GOME-2 AAI and the SCIAMACHY AAI, and (ii) the slope of the linear fit to the GOME-2 versus SCIAMACHY data points is close to one. On the other hand, a mild seasonal variation was found in the time series of the slope. It is possible that this seasonal variation is real, i.e., really present as a problem in the GOME-2 AAI data. But it could also be artificial, i.e., an artefact of the intercomparison itself. In the latter case the seasonal variation could be safely ignored. If the seasonal variation is real, however, then this could point to calibration problems in the level-1 data. Unfortunately, we cannot find out if the seasonal variation is "real" or "artificial". Note that the magnitude of the seasonal variation is very small. The offset between the GOME-2 AAI and the SCIAMACHY AAI is in general very small as well, indicating that there are at least no large and constant radiometric calibration problems involved.

The bias-corrected uncertainty in the GOME-2 AAI was found to be $\sim$0.5 index point. As explained in section 3.5, this is only an upper limit, because this value is also determined by the quality of the SCIAMACHY AAI and the quality of our intercomparison approach. In any case, the (bias-corrected) value of roughly 0.5 index points relates well to the target uncertainty of 0.5 index points mentioned in the O3M SAF Product Requirements Document (PRD) [*O3M SAF Project Team*, 2014]. Using the validation technique described in this chapter, it is not possible to reach a higher accuracy for the intercomparison results, and therefore it is impossible to assess whether or not the GOME-2 AAI could reach the PRD breakthrough level of 0.2 index points. This level might perhaps be reached, but this cannot be checked with the current intercomparison technique.

Please note that by using SCIAMACHY as a reference, the results in principle only apply to residues coming from the inner part of the GOME-2 swath, i.e., observations for which the viewing zenith angle (VZA) is below $\sim$33°. It is also important to mention again that we made use of forward pixels only. Backscan pixels were not taken into account in the analysis, and the results therefore only apply to the GOME-2 measurements that were performed in the forward scan of the instrument.

4 Reprocessed AAI products from MetOp-A

4.1 Time series of global mean AAI

Analysing the global mean residue is a simple and robust validation technique for the AAI [see, for instance, *de Graaf et al.*, 2005; *Tilstra et al.*, 2010, 2012a]. The daily global mean residue, in this report, is defined as the average of all healthy residue measurements on a day located between 60°N and 60°S and having solar zenith angles below 85 degrees. This global mean turns out to be a rather stable and predictable property, which is something we can use to validate the residue/AAI.

In this section we present results for the global mean residue for individual positions of the scanner mirror. For observations between 60°N and 60°S, the integration time is 187.5 ms, leading to 32 measurements per scan, of which the last 8 are backscan measurements. Despite the fact that the number of measurements over which is averaged decreases by a factor of 32 when we restrict ourselves to individual scanner mirror positions, we still end up with a statistical property which is stable enough for the time series analyses we will be performing in the rest of this validation report.

4.2 AAI from the Main Science Channels

4.2.1 Time series

In Figure 19 we present the GOME-2/MetOp-A daily global mean residue versus time for all forward scan mirror positions. There are 24 measurements inside each forward GOME-2 scan, resulting in 24 time series, each with their own colour and labelled by their own "IndexInScan" number. From Figure 19 it is clear that the effects of instrument degradation were removed successfully. Also compare with Figure 2. Several vertical lines are plotted in Figure 19. These are to indicate the times at which important instrumental events or software updates took place. The most important ones are (i) the change of the PMD band definition (from v1.0 to v3.1) that took place on 11 March 2008, (ii) the throughput test in January and September 2009, (iii) changes of unknown nature between 10 May 2010 and 27 December 2010, (iv) the swath width reduction (from 1920 km to 960 km) on 15 July 2013, and (v) the switch to level-1 processor version 6.1 that was executed on 25 June 2015. The two black lines in March 2013 indicate a period of one week during which the swath width was reduced for testing purposes. Most features can be linked to instrumental/software changes.

In Figure 20 we present the global mean residue as a function of scanner mirror position, for all available days in the months December and January. The colours can be related to the actual date using the colour bar. Note that the global mean AAI of the backscan pixels is displayed also. The vertical dotted line indicates the turning point of the motion of the scan mirror at the west side of the

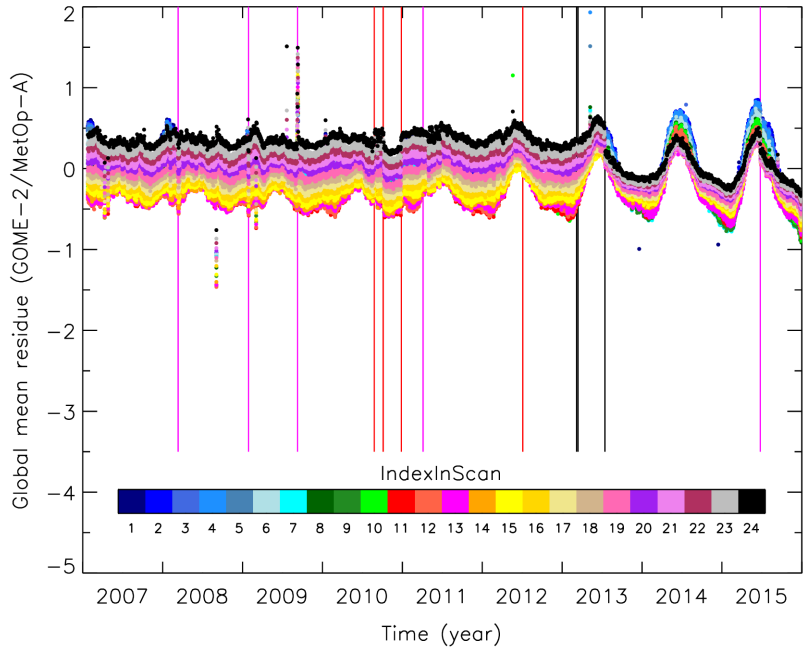

Figure 19: Daily global mean residue for all 24 forward scan mirror positions inside the GOME-2 swath plotted versus the time. The colours relate to the "IndexInScan" number, as indicated by the colour bar. A trend due to instrument degradation, as was seen in Figure 2, is absent.

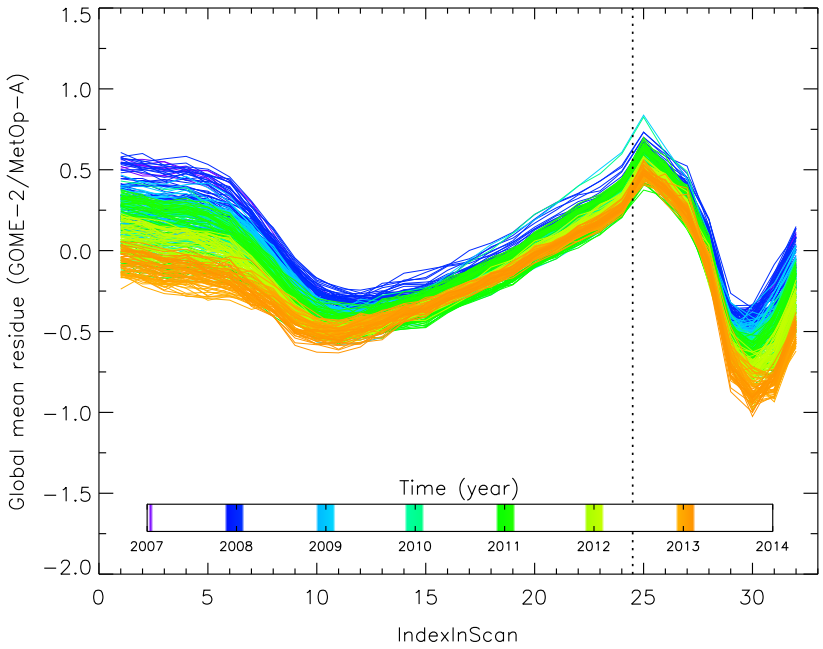

Figure 20: Global mean residue as a function of scanner mirror position, for all available days in the months December and January of the years up to 2013. The colours can be related to the actual date using the colour bar. The vertical dotted line illustrates the westernmost scanner angle position.

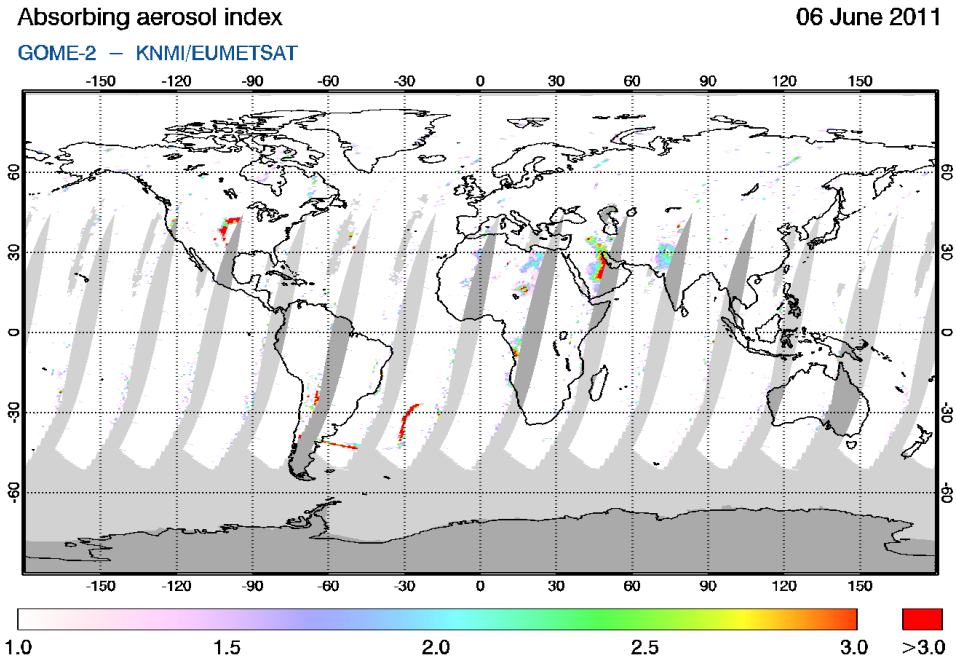

Figure 21: Global map of the AAI measured by GOME-2 on MetOp-A for 6 June 2011.

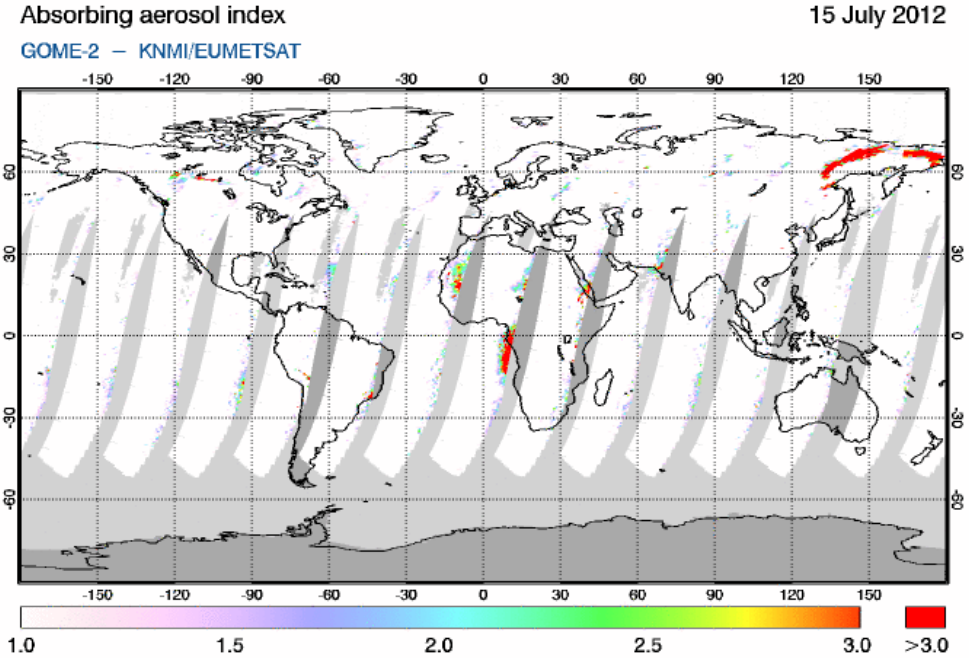

Figure 22: Global map of the AAI measured by GOME-2 on MetOp-A for 15 July 2012.

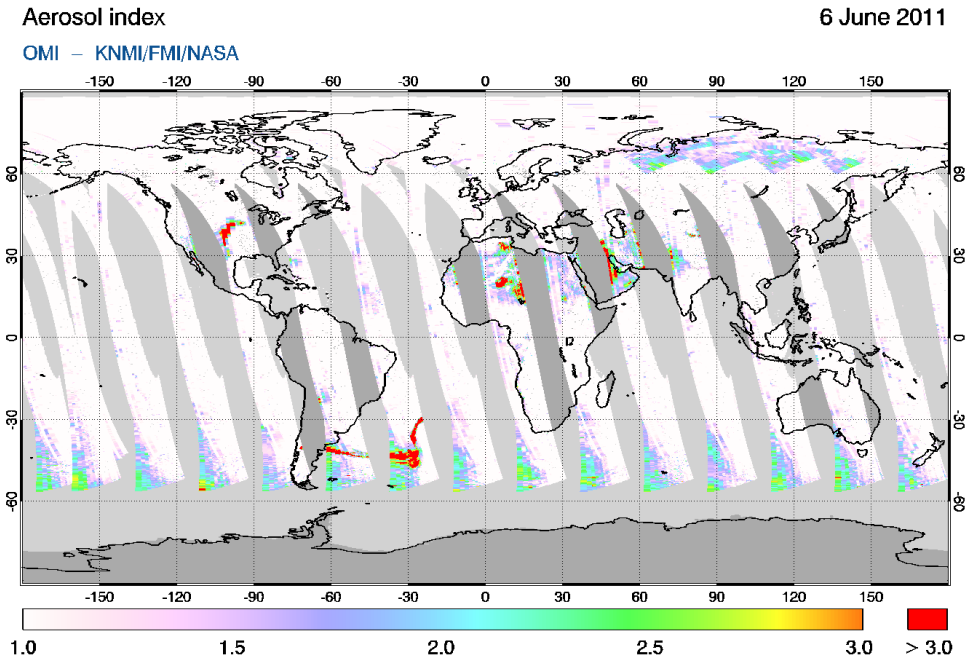

Figure 23: Global map of the AAI measured by OMI on the Aura satellite for 6 June 2011.

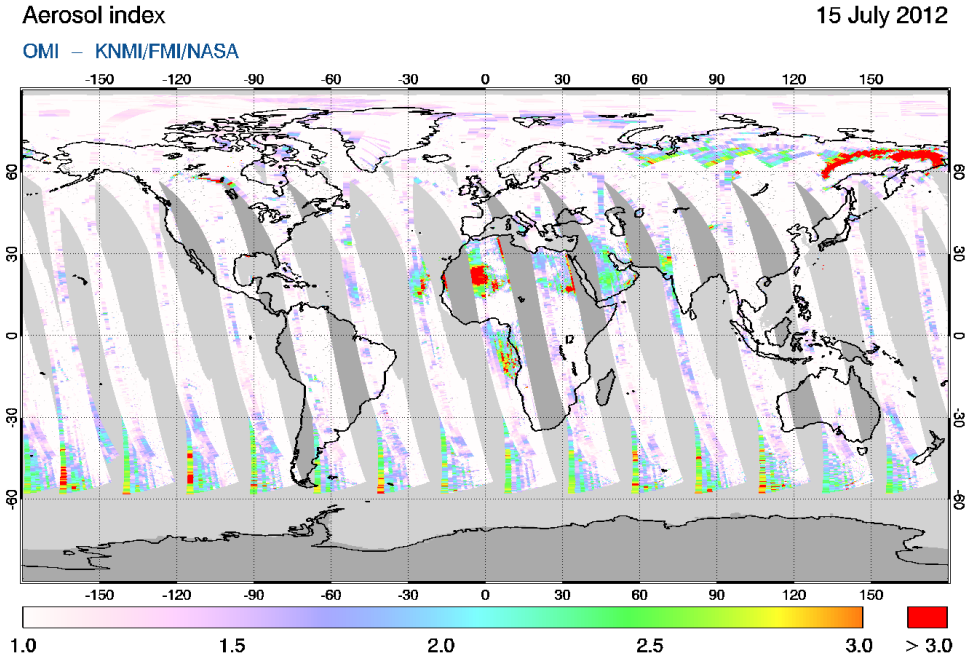

Figure 24: Global map of the AAI measured by OMI on the Aura satellite for 15 July 2012.

orbit swath. Data later than January 2013 were not plotted because of the swath width reduction that was executed on 15 July 2013. Figure 20 should be compared to Figure 3.

Note that the forward scan and the backward scan behave slightly differently. We would expect the backscan part to show the same behaviour as the forwards scan, at least when taking into account that the scanning direction is reversed and that the scan speed is three times as high. However, the minimum value achieved in the backward scan (-1.0 index points) is a bit lower than the minimum in the forward scan (-0.5), whereas the values at IndexInScan positions of 1 and 32 are different as well, even though they both relate to the eastern side to the swath. Part of this may be explained by the larger footprint size, but also the phenomenon of spatial aliasing has an impact.

Spatial aliasing causes the two wavelength of the 340/380-nm wavelength pair to be read out at different times. For instance, when the first detector pixel of spectral channel 3 starts accumulating the incoming radiation, the last detector pixel of the spectral channel starts doing the same exactly 46.875 ms later. For spectral channel 2, it is the other way around, and the first detector pixel is read out 46.875 ms later than the last detector pixel. For the two wavelengths 340 and 380 nm, both residing in spectral channel 2, the time difference is roughly half of that, i.e., on the order of 1/8th of the integration time. For the backscan pixels, the effect is three times as large because of the three times larger scan speed of the scanner mirror, and in the opposite direction. As a result, in one scanning direction the 340-nm viewing zenith angle (VZA) is larger than the 380-nm VZA, while in the other scanning direction the 340-nm VZA is smaller than the 380 nm VZA.

The 340-nm and 380-nm reflectances therefore observe slightly different scenes. The impact of differences in cloud presence and surface albedo would normally cancel out in the calculation of the global mean residues. The differences in the Rayleigh component of the backscattered light do not cancel out, however, because this is a systematic effect. Note that the AAI is strongly dependent on scattering geometry to begin with [*de Graaf et al.*, 2005]. In any case, there are differences between the forward scan and backward scan due to differences in pixel size and the spatial aliasing effect.

4.2.2 Images

In Figures 21 and 22 we present global maps of daily measurements of the MSC-AAI from GOME-2 on MetOp-A for 6 June 2011 and 15 July 2012, respectively. The first case (of 6 June 2011) shows an ash plume originating from the Puyehue-Cordón Caulle eruption and travelling across the South Atlantic Ocean. The second case (of 15 July 2012) shows biomass burning leaving the coast of West Africa, as well as strong smoke plumes from forest fires over eastern Russia. Figures 23 and 24 present the AAI from the OMI instrument for the same two days, for comparison. For the two special events, there is good agreement. The typical biomass burning and desert dust events are captured by the AAI from both satellite instruments, but the magnitude of the AAI differs somewhat.

4.3 AAI from the PMD bands

4.3.1 Short introduction of the PMD-AAI

For the MSC-AAI products the reflectances are determined from two wavelength bands in spectral channel 2 (centred at 340 and 380 nm). The size of the MSC measurement footprints amounts to roughly 80×40 km^2 for the largest part of the orbit. The AAI products derived from polarisation measurement device (PMD) band measurements are derived from reflectances measured by PMD-p bands 5 and 7, currently configured to wavelengths of 338 and 382 nm. The main advantage of the PMD-AAI product is the smaller footprint size, which amounts to roughly 10×40 km^2. For the validation of the PMD-AAI we follow basically the same procedure as for the MSC-AAI.

4.3.2 Time series

In Figure 25 we present time series of the global mean residue determined from PMD band measurements by GOME-2 onboard MetOp-A. Only a fraction of the 192 PMD scan mirror positions of the forward scan are shown (see colour bar). Data from before 11 March 2008 (indicated by the first vertical line) are not plotted because before this date the definition of the PMD bands was different. Data from before this date are therefore not consistent with data from after this date. As a result of this, PMD-AAI data from before the PMD band definition change are not made public.

The results are very comparable to those of the MSC-AAI. Some small differences are there, but these can be explained by the fact that there are differences in the wavelength definition of the PMD bands. The wavelengths of the PMD bands currently used are 338 (PMD 5) and 382 nm (PMD 7). For the MSC-AAI these wavelength were set to 340 and 380 nm, respectively. Also, calibration issues are known to be present in the reflectances retrieved by the PMD bands [*Tilstra et al.*, 2011]. Nevertheless, the agreement with the MSC time series is satisfactory.

Several vertical lines are plotted in Figure 25. These are to indicate the times at which important instrumental events or software updates took place. The most important ones for the PMD-AAI are (i) the change of the PMD band definition (from v1.0 to v3.1) that took place on 11 March 2008, (ii) the throughput test in January and September 2009, (iii) a PPF change executed on 3 July 2012, (iv) the swath width reduction (from 1920 km to 960 km) on 15 July 2013, and (v) the switch to level-1 processor version 6.1 that was executed on 25 June 2015. The two black lines in March 2013 indicate a period of one week during which the swath width was reduced for testing purposes.

In Figure 26 we present the same global mean PMD residue, but now as a function of scan mirror position. Backscan measurements are also shown, the scan mirror position therefore runs from 1 to 256. The vertical dotted line indicates the turning point, where the scan mirror changes direction

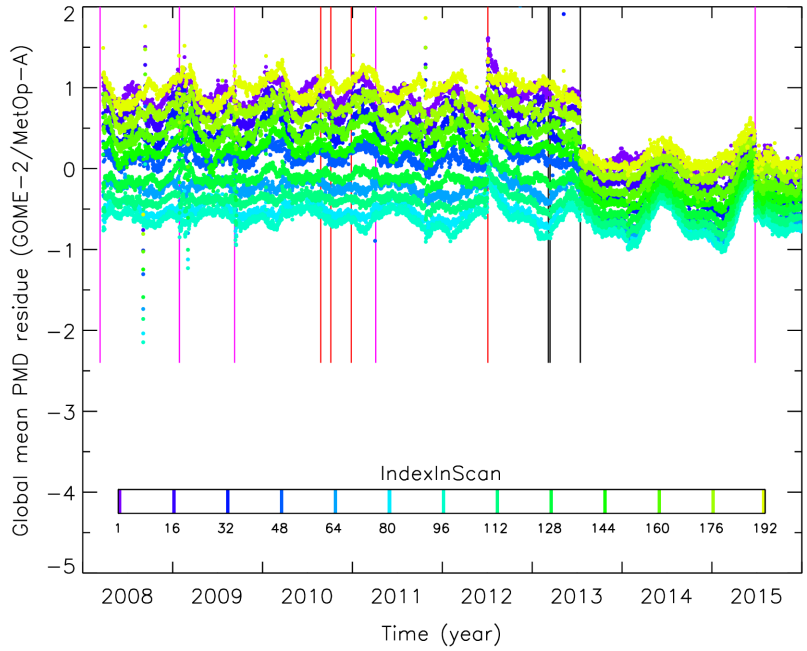

Figure 25: Daily global mean residue versus time for a selection of the 192 (forward scan) PMD scan mirror positions inside the GOME-2/MetOp-A orbit swath. The colours relate to the "IndexInScan" number, as indicated by the colour bar. Notice the swath width reduction (at 15 July 2013).

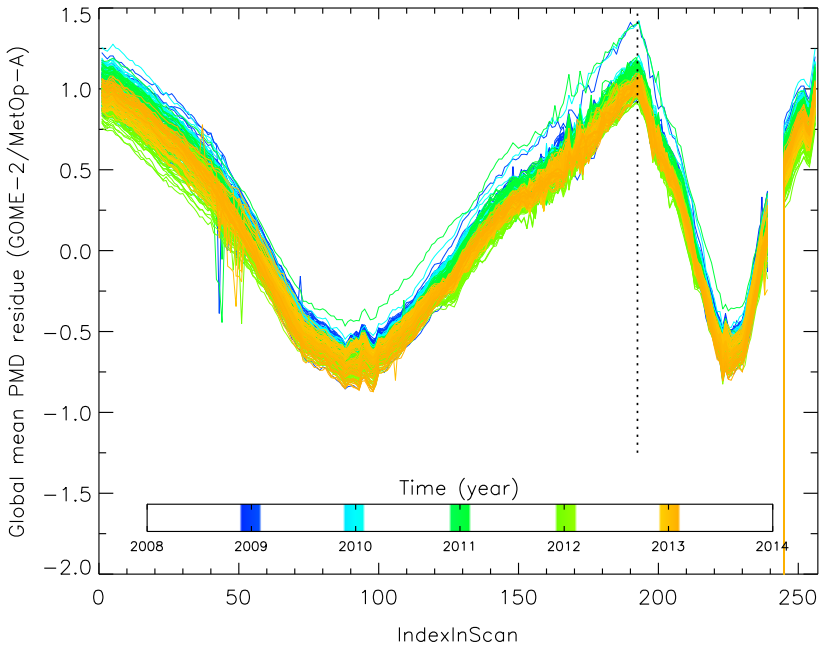

Figure 26: Global mean PMD residue measured by GOME-2 on the MetOp-A platform as a function of scanner mirror position. Compare with Figure 20. Data from before the PMD band definition change (11 March 2008) and from after the swath width reduction (15 July 2013) are not plotted.

of movement. Note that the retrieval at scan mirror positions 240–244 fails. Pixels 240–243 are known as reset pixels [*Munro and Lang*, 2011], and do not produce valid measurements. Pixel 244, next in line after the reset pixels, produces radiances which are not to be trusted. Note that these measurements are performed during the backscan of the instrument.

Note that the backscan pixels show the same behaviour as the forward scan pixels, taking into account that the scanning direction is reversed and that the scan speed is three times as high. This is an important difference w.r.t. the MSC-AAI, where this symmetry was broken (see section 4.2.1). The PMD footprints are much smaller than the MSC footprints, and the (relative) spatial aliasing effect between PMD bands 5 and 7 (used for the PMD-AAI) is much smaller because they are located close to each other in the PMD-p and PMD-s detector arrays [*EUMETSAT*, 2014].

Comparing Figure 26 with Figure 20 we conclude that there is a good agreement with the MSC-AAI product. The offset with respect to the MSC-AAI from GOME-2/MetOp-A is $\sim$0.3 index points over the entire time range. This offset of $\sim$0.3 index points is relatively small considering the fact that the AAI is very sensitive to changes and differences in radiometric calibration.

4.3.3 Images

The main advantage of the PMD-AAI over the MSC-AAI is the higher spatial resolution. The footprint size amounts to roughly 10×40 km^2. After the swath width reduction executed on 15 July 2013 the PMD footprint size became 5×40 km^2. In Figures 27 and 28 we present images of two aerosol events that are nicely recorded by the PMD-AAI. The first case (of 6 June 2011) is that of an ash plume originating from the Puyehue-Cordón Caulle eruption and travelling across the South Atlantic Ocean. The ash plume is captured extremely well by the PMD-AAI in three subsequent orbits. Also compare with Figure 21 which is a MSC-AAI global image of the same day.

The second case (of 15 July 2012) shows strong smoke plumes originating from forest fires over eastern Russia. Also compare with Figure 22. The high spatial resolution of the PMD-AAI makes it ideally suited for monitoring aerosol plumes from volcanic eruptions and forest fires.

4.4 Summary and conclusion

The validation of the MSC-AAI consisted of a pixel-to-pixel comparison with the SCIAMACHY AAI and statistical analyses of time series of global mean MSC-AAI. Both analyses confirmed that instrument degradation has been removed successfully, that is, no remnants of instrument degradation could be found. The MSC-AAI from MetOp-A turns out to be in good agreement w.r.t. the SCIAMACHY AAI. Only a very small difference of 0.2 index points was found.

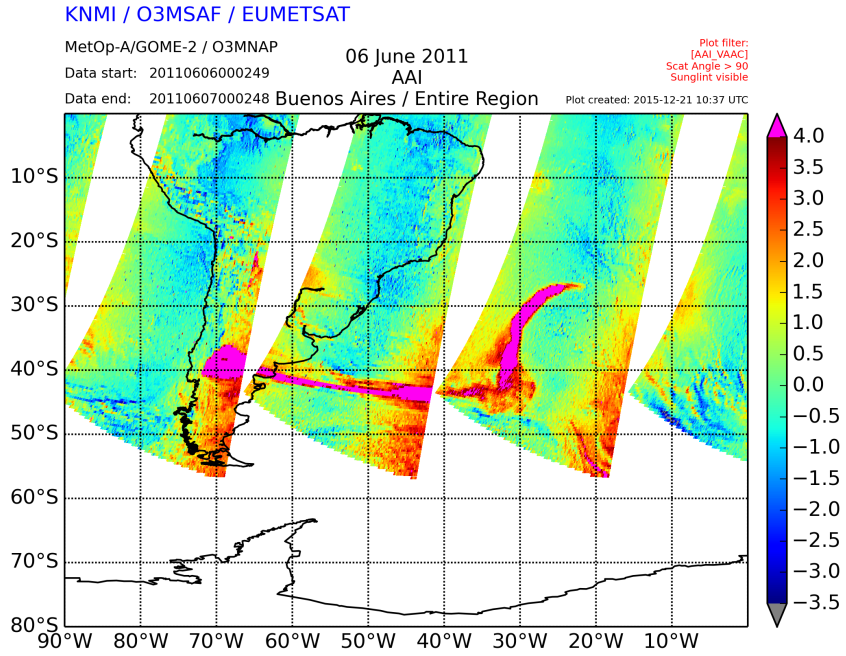

Figure 27: Map of the PMD-AAI measured by GOME-2 on MetOp-A for 6 June 2011. One can clearly identify the massive ash plume caused by the eruption of Puyehue-Cordón Caulle.

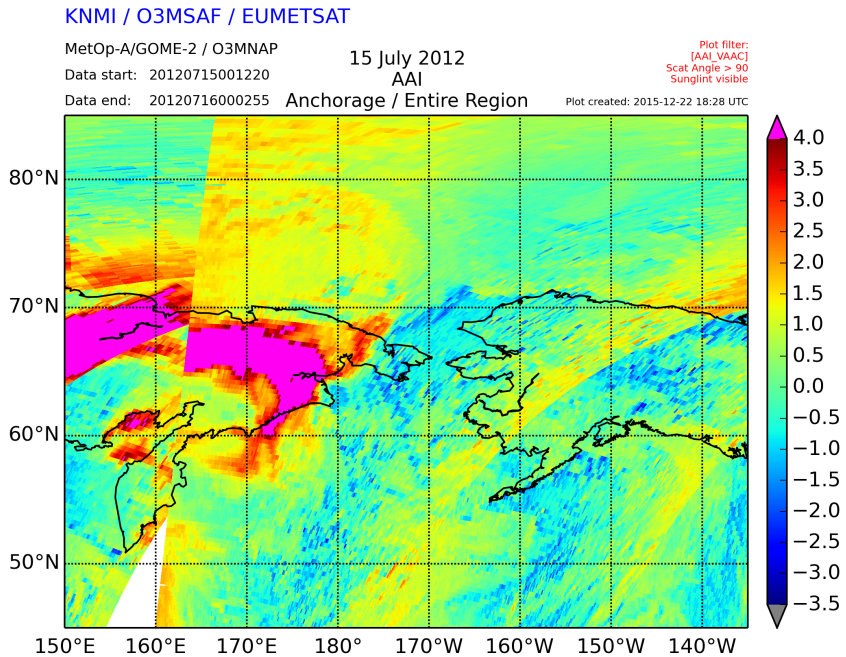

Figure 28: Map of the PMD-AAI measured by GOME-2 on MetOp-A for 15 July 2012. The ash plume, which was caused by forest fires over eastern Russia, is well captured by the PMD-AAI.

For the PMD-AAI no comparison with SCIAMACHY can be made because of the differences in wavelength pair. But, the analysis of the global mean PMD-AAI reveals behaviour identical to that of the global mean MSC-AAI. Again no remnants of instrument degradation could be found. The PMD-AAI is found to be very close the MSC-AAI: a difference of $\sim$0.3 index points was found.

5 Reprocessed AAI products from MetOp-B

5.1 AAI from the Main Science Channels

5.1.1 Time series

Time series of the global mean MSC-AAI from MetOp-B are presented in Figures 29 and 30. The time series shown in Figure 29 are very similar to the time series presented in Figure 20 for MetOp-A. However, a relatively small offset of about 0.3 index point is present in the GOME-2/MetOp-B AAI, caused by differences in the radiometric calibration of the two instruments. Looking at Figure 30 and comparing it to Figure 20 we conclude that the results for MetOp-A and MetOp-B are very similar.

5.1.2 Images

In Figures 31 and 32 we compare the MSC-AAI retrieved from GOME-2 on MetOp-B with the AAI retrieved by the OMI instrument on the same day. It should be noted that the OMI AAI is suffering from the so-called row-anomaly problem. Qualitatively, however, there is sufficient agreement.

5.2 AAI from the PMD bands

5.2.1 Time series

Time series of the global mean PMD-AAI from MetOp-B are presented in Figures 33 and 34. The time series shown in Figure 33 are very similar to the time series presented in Figure 25 for MetOp-A.

5.2.2 Images

In Figures 35 and 36 we compare the PMD-AAI retrieved from GOME-2 on MetOp-B with the AAI retrieved by the OMI instrument on the same day (29 June 2015). The ash plume, which is captured well by both instruments, is caused by forest fires. There is sufficient agreement. Note that the OMI AAI from recent years (end of 2008) has a reduced coverage due to the row-anomaly problem.

5.3 Summary and conclusion

The applied verification method is identical to the one adopted for MetOp-A. In all cases, the results for MetOp-B are very similar to the results found for MetOp-A.

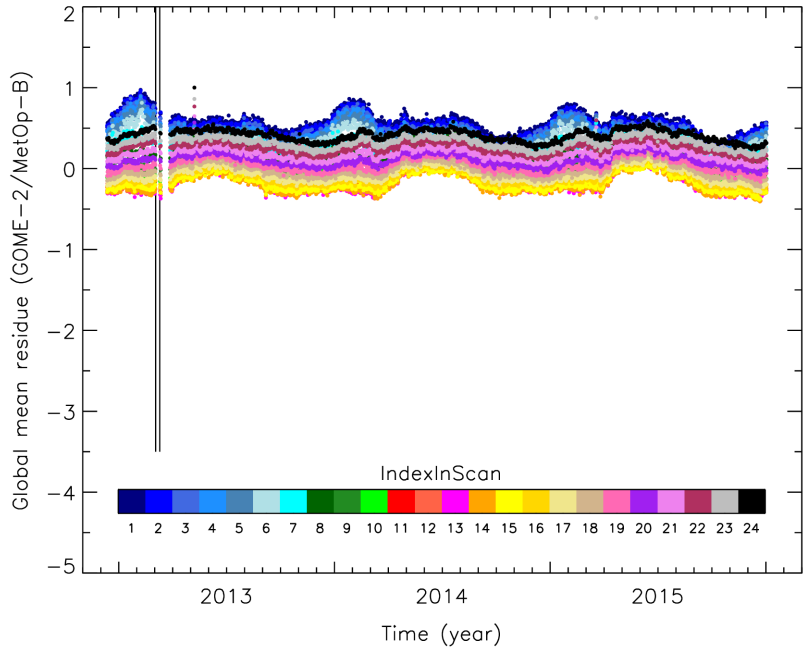

Figure 29: Daily global mean residue for all 24 forward scan mirror positions inside the GOME-2 swath plotted versus the time. The colours relate to the "IndexInScan" number, as indicated by the colour bar. A trend due to instrument degradation, such as seen in Figure 2, is absent.

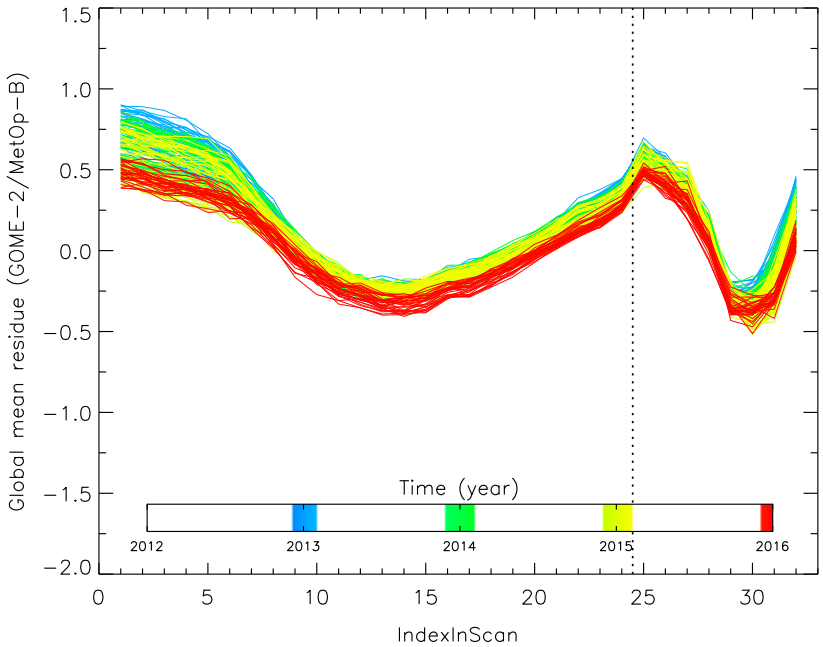

Figure 30: Global mean residue as a function of scanner mirror position, for all available days in the months December and January of the years up to 2013. The colours can be related to the actual date using the colour bar. The vertical dotted line illustrates the westernmost scanner angle position.

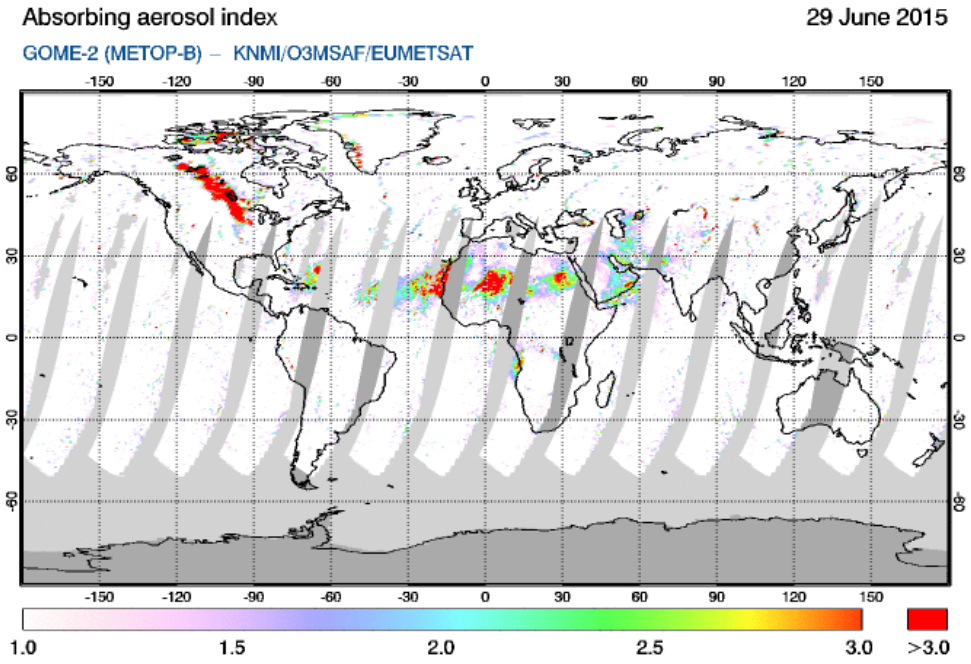

Figure 31: Global map of the MSC-AAI measured by GOME-2 on MetOp-B for 29 June 2015.

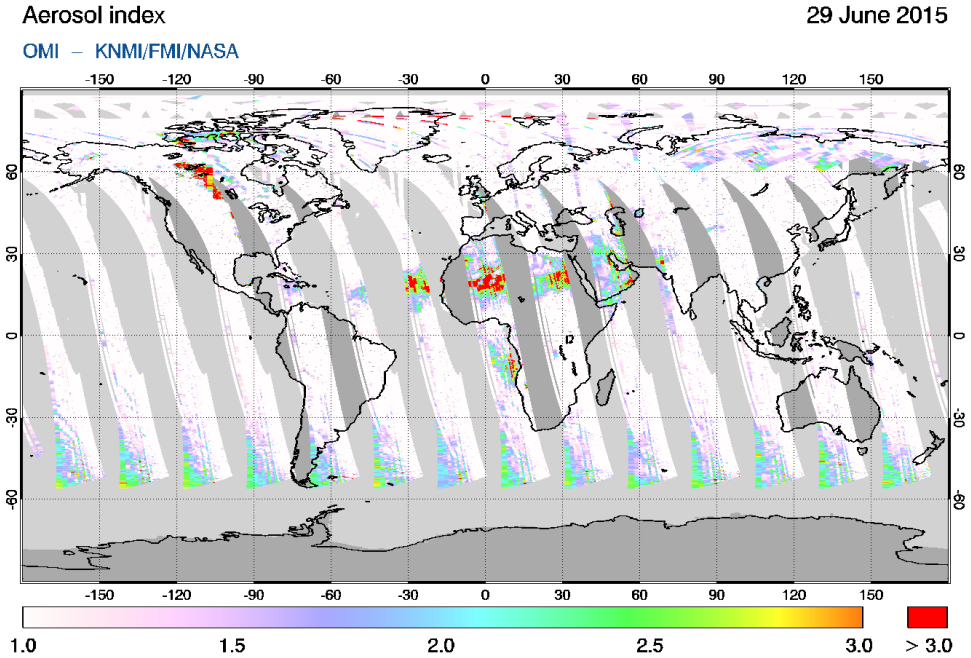

Figure 32: Global map of the AAI measured by the OMI instrument for 29 June 2015.

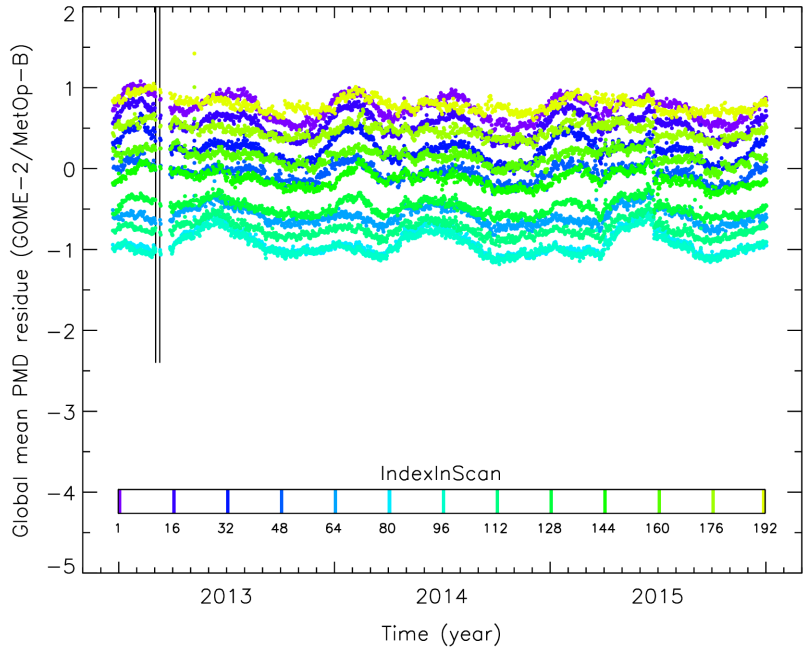

Figure 33: Daily global mean PMD-AAI residue for 24 selected (forward scan) scan mirror positions inside the GOME-2 on MetOp-B orbit swath plotted versus the time. The colours relate in the usual way to the "IndexInScan" number, indicated by the colour bar.

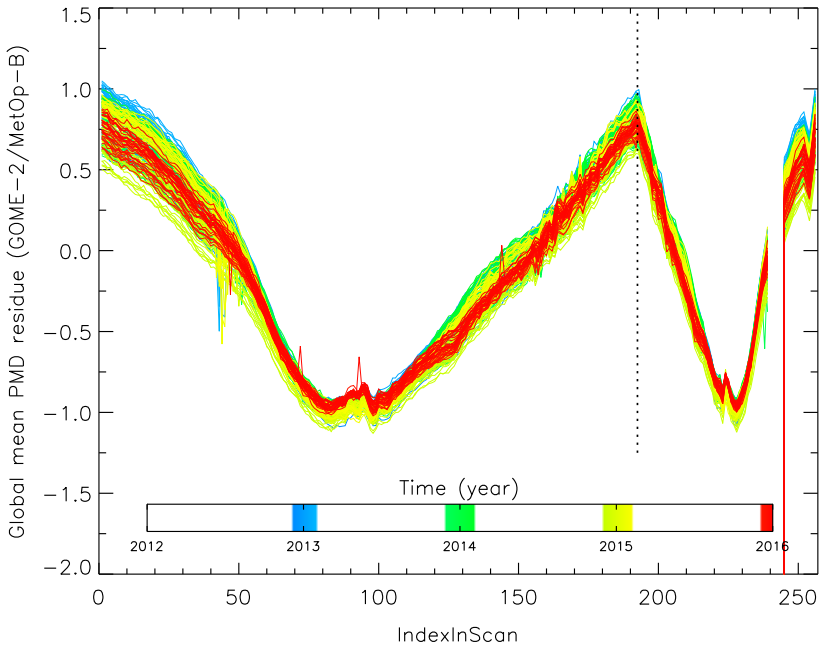

Figure 34: Global mean PMD-AAI residue versus scan mirror position, for all available days in the months December and January of the years up to 2013. The colours can be related to the actual date using the colour bar. The vertical dotted line illustrates the westernmost scanner angle position.

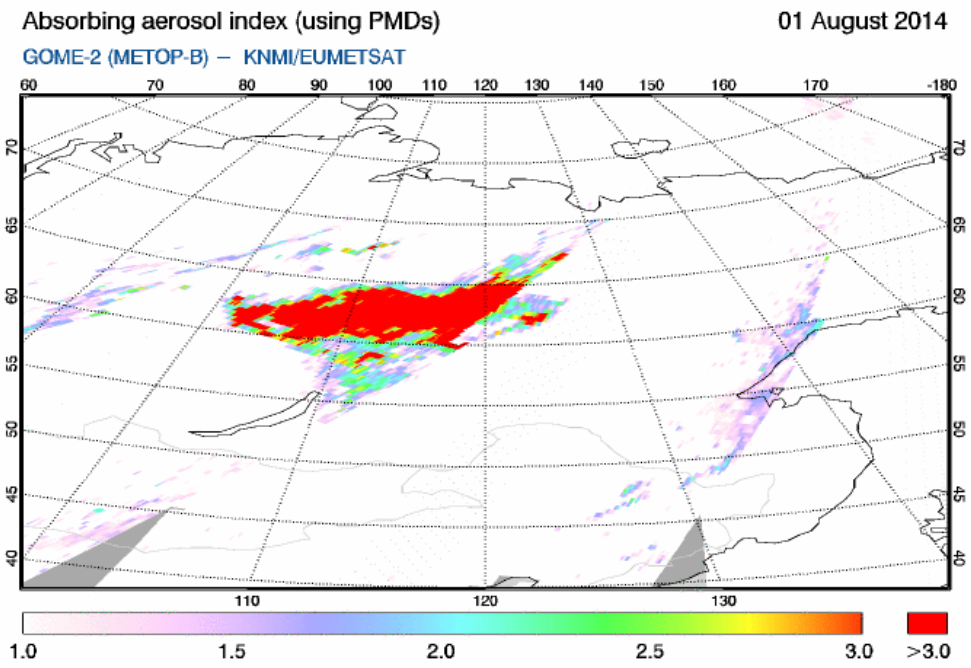

Figure 35: Global map of the PMD-AAI measured by GOME-2 on MetOp-B for 1 August 2014.

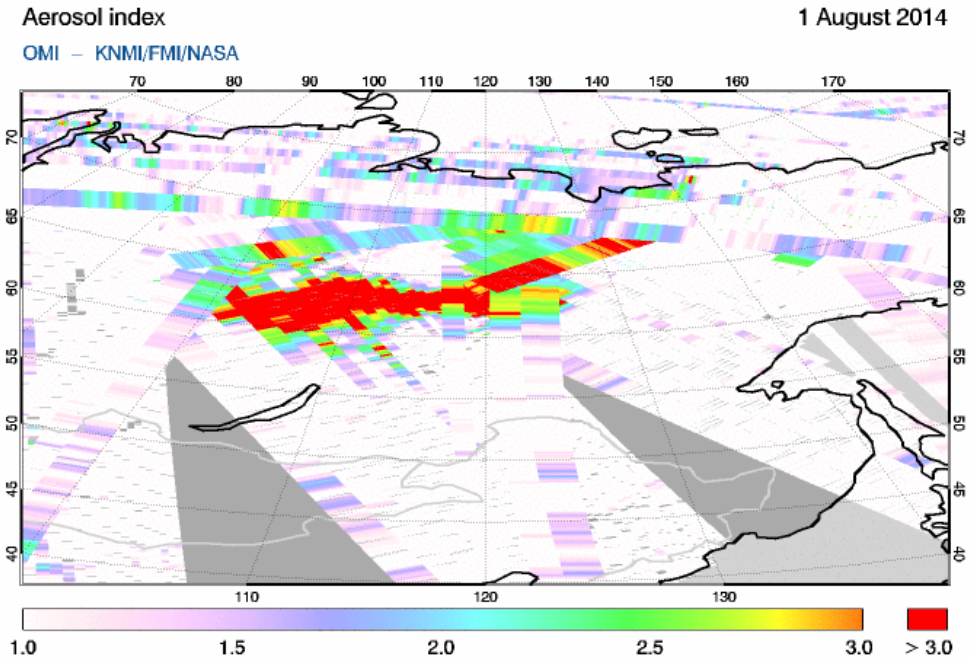

Figure 36: Global map of the AAI measured by the OMI instrument for 1 August 2014.

6 Summary and conclusions

From comparison with the SCIAMACHY AAI we conclude that the MSC-AAI from GOME-2 on MetOp-A is well calibrated. All products that were investigated (MSC-AAI and PMD-AAI, both for MetOp-A and MetOp-B) behave as they should.

Time series of the global mean residue show that the correction for instrument degradation is successful. The analyses show that the year-to-year variation of the global mean of the AAI does no longer suffer severely from the impact of instrument degradation. Features like the increased seasonal amplitude in the global mean AAI from GOME-2 on MetOp-A, visible after the year 2012, cannot be removed by our correction for instrument degradation. This is because our current correction handles drifts in the radiometric calibration using a low order polynomial representative for progressively evolving optical instrument degradation.

Differences between the MSC-AAI and PMD-AAI exist, but they are small. The differences between the AAI products from MetOp-A and those from MetOp-B are relatively small.

References

Bovensmann, H., J. P. Burrows, M. Buchwitz, J. Frerick, S. Noël, V. V. Rozanov, K. V. Chance, and A. P. H. Goede (1999), SCIAMACHY: Mission objectives and measurement modes, *J. Atmos. Sci., 56*(2), 127–150.

de Graaf, M., P. Stammes, O. Torres, and R. B. A. Koelemeijer (2005), Absorbing Aerosol Index: Sensitivity analysis, application to GOME and comparison with TOMS, *J. Geophys. Res., 110*, D01201, doi:10.1029/2004JD005178.

EUMETSAT (2014), GOME-2 Factsheet, Doc. No. EUM/OPS/DOC/10/1299, Issue 4a, 20 May 2014, EUMETSAT, Darmstadt, Germany.

Herman, J. R., and E. A. Celarier (1997), Earth surface reflectivity climatology at 340–380 nm from TOMS data, *J. Geophys. Res., 102*(D23), 28,003–28,011, doi:10.1029/97JD02074.

Munro, R. and R. Lang (2011), GOME-2 Level 1 Product Generation Specification, Doc. No. EPS.SYS.SPE.990011, Issue 7.0, 28 February, EUMETSAT, Darmstadt, Germany.

O3M SAF Project Team (2014), O3M SAF Product Requirements Document, Doc. No. SAF/O3M/FMI/RQ/PRD/001, Issue 1.6, 3 December 2014, EUMETSAT, Darmstadt, Germany.

Tilstra, L. G., M. de Graaf, I. Aben, and P. Stammes (2007), Analysis of 5 years SCIAMACHY Absorbing Aerosol Index data, in *Proceedings of the 2007 Envisat Symposium*, ESA Special Publication SP-636, European Space Agency, Noordwijk, The Netherlands.

Tilstra, L. G., M. de Graaf, I. Aben, and P. Stammes (2012a), In-flight degradation correction of SCIAMACHY UV reflectances and Absorbing Aerosol Index, *J. Geophys. Res., 117*, D06209, doi:10.1029/2011JD016957.

Tilstra, L. G. M. de Graaf, O. N. E. Tuinder, R. J. van der A, and P. Stammes (2011), Studying trends in aerosol presence using the Absorbing Aerosol Index derived from GOME-1, SCIAMACHY, and GOME-2, in *Proceedings of the 2011 EUMETSAT Meteorological Satellite Conference*, EUMETSAT P.59, Oslo, Norway.

Tilstra, L. G., O. N. E. Tuinder, and P. Stammes (2010), GOME-2 Absorbing Aerosol Index: statistical analysis, comparison to GOME-1 and impact of instrument degradation, in *Proceedings of the 2010 EUMETSAT Meteorological Satellite Conference*, EUMETSAT P.57, ISBN 978-92-9110-089-7, Cordoba, Spain.

Tilstra, L. G., O. N. E. Tuinder, and P. Stammes (2012b), Introducing a new method for in-flight degradation correction of the Earth reflectance measured by GOME-2, and application to the AAI,

in *Proceedings of the 2012 EUMETSAT Meteorological Satellite Conference*, EUMETSAT P.61, Sopot, Poland.

Torres, O., P. K. Bhartia, J. R. Herman, Z. Ahmad, and J. Gleason (1998), Derivation of aerosol properties from satellite measurements of backscattered ultraviolet radiation: Theoretical basis, *J. Geophys. Res., 103*(D14), 17,099–17,110, doi:10.1029/98JD00900.